1-30-2013

S band narrow-wall slotted waveguide antenna For high-power applications

Xuyuan Pan

Xuyuan Pan

Candidate

Electrical & Computer Engineering

Department

This thesis is approved, and it is acceptable in quality and form for publication:

Approved by the Thesis Committee:

Dr. Christos Christodoulou , Chairperson

Dr. Edl Schamiloglu

Dr. Joseph Costantine

S band Narrow-wall Slotted Waveguide Antenna For High-power Applications

by

Xuyuan Pan

B.S., University of Xidian, 2011

THESIS

Submitted in Partial Fulfillment of the

Requirements for the Degree of

Master of Science
Electrical Engineering

The University of New Mexico

Albuquerque, New Mexico

December, 2012

Dedication

To my loving parents, Zhaichun Pan and Naiqin Tong for all the unconditional support and encouragement.

Acknowledgments

I would like to thank my advisor, Dr. Christos Christodoulou for accepting me as his Master student and giving the opportunity to work on this research project. I am honored and humbled for having been able to work under his supervision. I thank him for encouraging me to work on the project and offering me the facility and equipments to do experiments. I am also very thankful to Dr. Christodoulou for financially supporting me through my Master program. I thank Dr. Edl Schamiloglu for being on my committe and offering the equipments for me to fabricate the experiment model.

I thank Dr. Naga Ravi Kanth Devarapalli for the previous idea and design of the narrow-wall longitudinal-slot array. I am very thankful to Dr. Devarapalli for many useful discussions about the design method, which is essential for me to be able to finish this work in this time frame. I am also thankful to Dr. Devarapalli for his dissertation and other research documents, which expedite the process of my work.

I thank Dr. Joseph Costantine for being on my committee and for some useful suggestions for my research. I thank Dr. Youssef Tawk for the guidance to start this research work and the suggestions for my further research. I thank my colleague and friend, Mr. George Atmatzakis for his knowledge of all the equipments and the help to my experiments. I thank my colleague and friend, Mr. Firas Ayoub for the help with the experiments. I thank my colleague, Mr. Brock Franklin Roberts for his help with the fabrication of the experiment model. I thank Miss Carlyn Pinkins for her criticism about my work and her suggestions for my thesis modification.

This research was sponsored by U.S. Office of Naval Research Grant ONR N00014-09-1-1084, Lee Mastroianni, Program Manager. [1]

[1]To my family and friends, who are the nicest people I ever know

S band Narrow-wall Slotted Waveguide Antenna For High-power Applications

by

Xuyuan Pan

B.S., University of Xidian, 2011

M.S., Electrical Engineering, University of New Mexico, 2012

Abstract

This work seeks designs of novel antennas, such as the rectangular waveguide narrow-wall longitudinal-aperture antenna arrays for S band high power applications. This antenna is designed to perform as a uniform array with minimum power reflected into the feed-waveguide. Based on the configuration, the double-narrow-wall-slot-array design is proposed for higher gain and grating lobes suppression. This work also deals with the S band compact narrow-wall slot-array proposed to be rendered as a conformal antenna structure. Moreover, this work proposes a circularly polarized narrow-wall longitudinal-aperture array design to produce both vertically and horizontally polarized radiated power. In the end, this work presents and discusses a couple of mechanisms for beam-steering of S band narrow-wall longitudinal-aperture array designs.

The S-band narrow-wall longitudinal-aperture array design consists of four narrow wall longitudinal-slot radiators and one H-plane-bend-radiator. The design is a combination of computational and microwave network analysis techniques. First, HFSS is used to analyze the S-parameters, phases and radiated power of the narrow-wall longitudinal-slot radiators as well as the H-plane-bend radiator. Second the

microwave network is applied to design a uniform linear array by neglecting the external coupling between the elements. Finally, Full-wave analysis is used to validate the array design from microwave network analysis.

The double-narrow-wall slot-array design is the best narrow-wall longitudinal-slot array design with a peak gain of approximately 15dB. It consists of two identical narrow-wall-slot-arrays with a common broad wall. It has a much more uniform aperture electric field distributuion than the single array design. As a result, a higher gain with suppressed grating lobes is achieved.

The S-band curved rectangular waveguide narrow-wall longitudinal-aperture antenna is proposed to perform as a conformal antenna structure. It is based on a rectangular waveguide bend so that it can be mounted easily on vehicles. It also consists of four narrow-wall longitudinal radiators and one H-plane-bend-radiator similar to the narrow-wall longitudinal slot-array.

A circularly polarized narrow-wall longitudinal-aperture array design is also discussed. It produces both vertically and horizontally polarized radiated power. The configuration verified by simulation places adjacent narrow-wall longitudinal radiators orthogonally and keeps the centers of all four narrow-wall longitudinal radiators at the same level.

A study of beam-steering capability is also conducted. It is divided into two parts. One moves the main beam on the plane orthogonal to the narrow-wall and orthogonal to the broad-wall of the rectangular waveguide. The other moves the main beam on the plane orthogonal to the narrow-wall and parallel to the broad-wall of the rectangular waveguide. The S-band narrow-wall longitudinal-slot array design works well both ways.

Finally, the experiment is designed and conducted to validate the theoretical analysis results for the design of S-band narrow-wall longitudinal-slot array. The

results obtained lead to the conclusion that there is good agreement between the theoretical and experiment results.

Contents

List of Figures

List of Figures

List of Tables

Chapter 1

Introduction

1.1 Overview

This work seeks to design and tests novel antennas, such as rectangular waveguide narrow-wall longitudinal-aperture antenna arrays for S band high power applications. The model of the antenna is chosen to fit potential applications requiring high average and high peak power sources. The best S band narrow-wall longitudinal-aperture array design is called the double-narrow-wall-slot-array. This work also deals with S band curved rectangular waveguide narrow-wall longitudinal-aperture antenna and circularly polarized narrow-wall longitudinal-aperture array design. Finally, the study of the capability of beam-steering of S band narrow-wall longitudinal-aperture array designs is conducted.

1.2 Thesis Motivation

Most suitable antenna types for high power applications are reflector and waveguide antennas. In addition to the ability to handle high powers, two essential requirements for a high power antenna are high directivity and low reflected power into the source.

To achieve a high gain, the dimension of a reflector antenna design is quite big, which makes it less conformal and exhibits higher wind resistance than, for example, a waveguide slotted array that can handle high powers and achieve a high gain. An air-filled waveguide antenna is more rugged than a reflector antenna. Unlike the waveguide antenna, taking out one part of a reflector antenna can make it powerless. The waveguide antenna is an air-filled rectangular waveguide slot array; the slots are longitudinal and in the narrow wall of waveguide as shown in Figure 1.1(a). The basic idea for the slot array is described in [1] [2].

The required radiation pattern along with the polarization of the electric field for this kind of high power antenna is shown in Figure 1.1(b). There are two reasons for having longitudinal-slots in the narrow wall of the waveguide. First, the configuration shown in Figure 1.1(a) is well suited to achieve the radiation pattern and the electric field polarization shown in Figure 1.1(b). Second, having slots in the narrow wall of a rectangular waveguide has its advantage to improve the power handling capabilities of the antenna.

For the dominant (TE_{10}) mode of operation for the rectangular waveguide, both the tangential and the normal component of E-field at the narrow-wall is zero. This behavior has been used by Taylor and Giri [3] to design a narrow-wall directional coupler for high power. The existence of a slot in the narrow-wall presents discontinuity to the propagating mode inside the waveguide and induces an aperture E-field as shown in Figure 1.1(a).

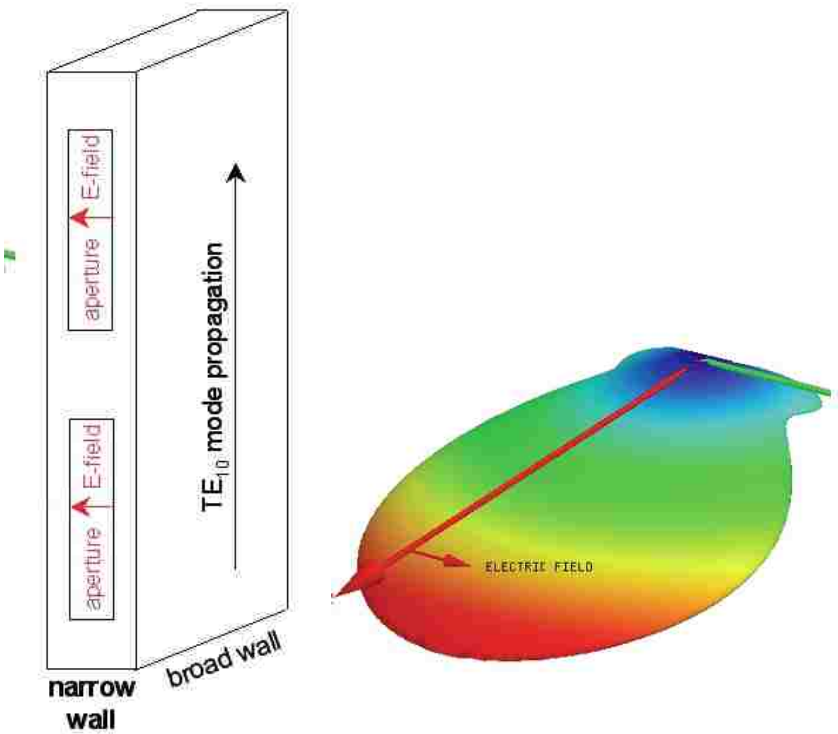

(a) (b)

Figure 1.1: (a)Schematic of the narrow-wall longitudinal-slot array (b) Fan beam radiation pattern with the radiated E-field direction produced by the narrow-wall longitudinal-slot array in Figure 1.1(a).

All the high power waveguide antenna arrays designed/tested in this work present similar fan beam radiation patterns with the E-field polarized along the broad dimension of the fan beam pattern as shown in Figure 1.1(b).

The required operating frequency for the narrow-wall longitudinal-slot array is required to be in the S band. The design of the S-band antenna is accomplished by evaluating and scaling of an X-band antenna developed in [4]. Based on this S-band narrow-wall longitudinal-slot arry, a couple of additional designs are proposed, as double-narrow-wall-slot-array, curved-narrow-wall-slot-array and circularly polarized narrow-wall-slot-array. Also beam-steering capability of this S-band narrow-wall

longitudinal-slot array is studied.

1.3 Organization of this Thesis

This work is divided into the following six chapters. The first chapter is the brief introduction to this work. The second chapter illustrates the analysis of individual elements in the array. It includes the characterization of a generic longitudinal-slot in the narrow wall of a rectangular waveguide and the design of a novel structure used as the last element of the narrow-wall longitudinal-slot array that enhances the array's performance. The third Chapter describes the design of the narrow-wall longitudinal-slot array using microwave network analysis and full-wave computational analysis. Chapter Three also includes the power handling ability analysis of the narrow-wall longitudinal-slot array. The fourth Chapter describes a couple of additional designs of the narrow-wall longitudinal-slot array. The fifth chapter describes the validation of the theoretical results through experiments. The sixth chapter describes the future work of improving the beam steering mechanism of the narrow-wall longitudinal-slot array antenna and the possibility of improving the design of narrow-wall longitudinal-slot array antenna for better circularly polarization as well as higher gain.

Chapter 2

Element Analysis

This section discusses the behavior of the individual array elements. Given that power handling is an important criterion in this study, narrow-wall slots with widths comparable to their lengths are considered. Ansoft Corporation's High Frequency Structrue Simulator(HFSS) is used for the analysis. The generic slot under consideration is a rounded rectangular slot in the narrow wall of a WR-284 waveguide, as shown in Figure 2.1.

2.1 S-band Narrow-wall Longitudinal-slot radiator

An equivalent transmission line model is used to study rectangular waveguide slot arrays [5], [6]. Traditional models assume that the slots are narrow, which was quantified by Equation 2.1; this is in addition to the consideration that the

$$2 \ log(\frac{length \ of \ slot}{width \ of \ slot}) \gg 1 \tag{2.1}$$

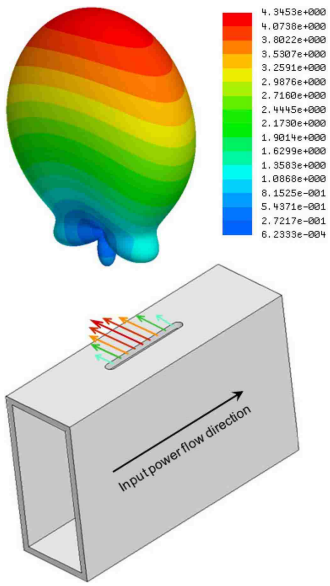

Figure 2.1: Generic narrow-wall longitudinal-slot with its aperture electri-field distribution and the 3-D absolute gain in dimensionless units.

waveguide is operating in the dominant (TE_{10}) mode. However, this consideration decreases the power handling capability of slot arrays, especially if the slots are in the broad wall of the waveguide. Hence, Equation 2.1 is violated for the slots in the proposed design of the radiator. Theoretical analysis becomes intractable for such slots and as a result, computational electromagnetic analysis is preferred.

2.1.1 Small aperture in the narrow wall of a rectangular waveguide

The scattering analysis of an aperture with dimensions small compared to a wavelength in a ground plane has already been performed in [7]. The polarizabilities of different shaped apertures have been found using the analysis in [8]. These expressions can be conveniently used to study the radiation characteristics of the apertures. The (electric/ magnetic) polarizability of an object is the dipole moment induced in

per unit (electric/ magnetic) field intensity incident upon it. Hence the electric (magnetic) polarizability, α_e (α_m) and the electric (magnetic) field current, $\vec{J}$ ($\vec{M}$) in the slot; i.e. the scattered fields radiated by the slot problem are the same when the slot is replaced by a perfect electric (magnetic) conductor with the equivalent electric (magnetic) current on it. Assuming that a rectangular waveguide is operating in the dominant (TE_{10}) mode, the tangential as well as the normal components of the E-field at its narrow wall are zero; hence only the magnetic terms, α_m, $\vec{M}$ need to be considered to find the far fields radiated by the narrow longitudinal-slot with dimensions small compared to a wavelength in the narrow wall of a rectangular waveguide. The polarizability of a small and narrow longitudinal slot in the narrow wall of a rectangular waveguide can be used, as described in this section, to find the radiated power in the far field by the longitudinal slot.

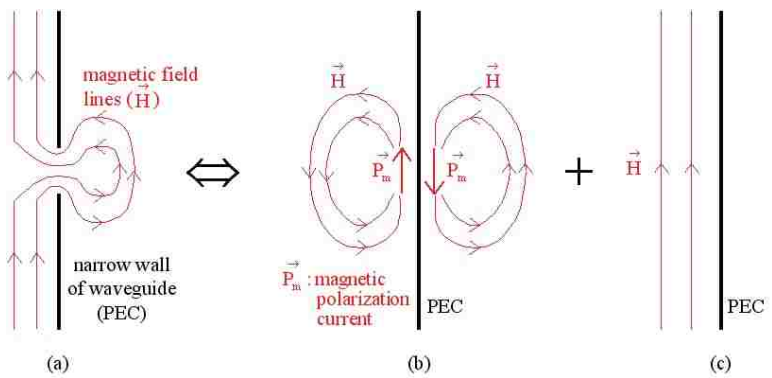

Figure 2.2: Small aperture in the narrow wall of a rectangular waveguide.

Figure 2.2(a) shows a partial view of a rectangular waveguide with a small aperture in its narrow wall. The propagating mode inside the waveguide is the dominant (TE_{10}) mode and the length of the slot is very small compared to the guide wavelength. The problem in figure 2.2(a) can be expressed as a superposition of the two problems shown in Figure 2.2(b), 2.2(c). Hence the radiation problem in Figure 2.2(a) reduces to the one shown in Figure 2.3, where $\vec{x}$, $\vec{y}$, $\vec{z}$ are the unit vectors in

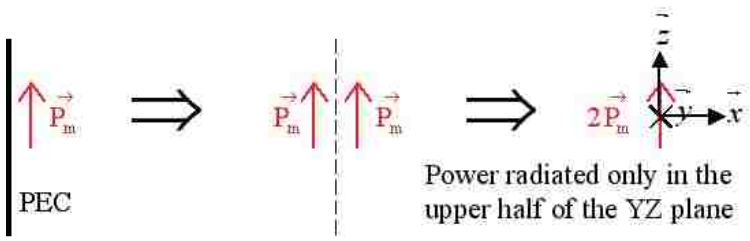

Figure 2.3: Radiation problem for the small aperture in Figure 2.2.

Cartesian coordinate system.

The magnetic polarization current ($\vec{P_m}$) in Figure 2.3 is given by Equation 2.2 [9].The equivalent magnetic current ($\vec{M}$) that is used to find the radiated fields is related to the magnetic polarization current as given by Equation 2.3.

$$\vec{P_m} = -\alpha_m \vec{H_{10}} \delta(x)\delta(y)\delta(z) \tag{2.2}$$

Where:

α_m is the magnetic polarizability of the small aperture in Figure 2.2(a)

$\vec{H_{10}}$ is the magnetic field intensity of the propagating TE_{10} mode inside the waveguide.

δ is the Dirac delta function

$$\vec{M} = 2j\omega\mu_0 \vec{P_m} \tag{2.3}$$

where:

ω is the angular frequency of operation

μ_0 is the permeability of free-space

The reason for the factor of two in Equation 2.3 is illustrated in Figure 2.3 and results in image theory.

Considering that the small aperture shown in Figure 2.2(a) is a narrow longitudinal slot, the magnetic polarizability (α_m) is given by Equation 2.4 [8].

$$\alpha_m = \frac{\pi}{24}\frac{l^3}{ln\frac{4l}{w} - 1} \tag{2.4}$$

where:

λ is the free space wavelength

l is the length of the slot and satifies the condition: $l \ll \lambda$

w is the width of the slot and satifies the condition: $w \ll \lambda$

Hence the electric and magnetic fields and the power radiated in the far field of the small longitudinal-slot in the narrow wall of a rectangular waveguide with only the dominant TE_{10} propagating mode inside are given as follows. The electric vector potential ($\vec{F}$) can be found from the magnetic current ($\vec{M}$); the radiated electric field ($\vec{E_r}$) and magnetic field ($\vec{H_r}$) can be found from $\vec{F}$; the power radiated in the far field ($\vec{P_r}$) can be found from $\vec{E_r}$, $\vec{H_r}$. The reference coordinate system used for these results is shown in Figure 2.3.

$$\vec{F} = -jF_z cos\theta \frac{e^{-j\beta r}}{r}\vec{r} + jF_z sin\theta \frac{e^{-j\beta r}}{r}\vec{r} \tag{2.5}$$

where:

$$F_z = \frac{\omega\epsilon_0\mu_0}{48}\frac{l^3 A_{10}}{ln(\frac{4l}{\omega}) - 1} \tag{2.6}$$

A_{10} is the magnitude of $\vec{H_{10}}$

$\vec{r}, \vec{\theta}, \vec{\phi}$ are the unit vectors in the Spherical coordinate system

r, θ, ϕ are the spatial variables in the Spherical coordinate system

$$\vec{E_r} = \omega\eta_0 F_z sin\theta \frac{e^{-j\beta r}}{r}\vec{\phi} \tag{2.7}$$

where:

η_0 is the impedance of free space

$$\vec{H_r} = -j\omega\vec{F} \tag{2.8}$$

$$\vec{P_r} = \frac{\pi}{6}\eta_0(\frac{\beta}{24}\frac{l^3 A_{10}}{ln(\frac{4l}{\omega}) - 1})^2 \tag{2.9}$$

where:

β_0 is the free space wave number.

2.1.2 S-band Narrow wall longitudinal-slot radiator

Although the theoretical analysis of small apertures exists, there is very little discussion available when the aperture dimensions are comparable to one wavelength and the slot width (w) is not negligible in comparison with the slot length (l). The analytical approach becomes intractable under this condition. The work in this section deals with the characterization of slots with aperture width comparable to the length, in the narrow wall of a rectangular waveguide, using computational techniques. The generic slot under consideration is shown in Figure 2.1.

The aim of this discussion is to generate intuition into the behavior of rectangular waveguide narrow-wall longitudinal-slots by presenting the extensive similarities they possess with a very well-known antenna. In addition, new insights into the behavior

of these slots can be achieved through the study of the relationships between the following parameters: the magnitude/phase of the power radiated by the slot, versus, the magnitude/phase of the reflected/transmitted power through the waveguide. The phase of the power radiated by the slot is proportional to the aperture phase at the center of the slot, which is defined as the phase of the electrical field at the center of the slot, with reference to the phase of the input power which is set to be 0^o at the input port of the element. The computational analysis was performed with the aid of Ansoft Corporation's High Frequency Structure Simulator (HFSS). Full wave analysis using HFSS was performed for various values of lengths and widths of a rounded rectangular shaped longitudinal-slot in the narrow wall of an S-band waveguide operating at 3.17GHz. Only part of this data was used in Chapter 3 for designing a narrow-wall longitudinal-slot array comprising of these slots due to the following reason. A half sine wave aperture E-field distribution is maintained only for certain slot dimensions, specifically for all possible widths as long as the length of the slot satisfis the condition in Equation 2.10.

$$l \leq \lambda/2 \tag{2.10}$$

The narrow-wall longitudinal-slot is first examined by comparing its properties to cylindrical wire antennas, where the width (length) of the slot is analogous to the diameter (length) of the wire. Slot radiators that satisfy the condition have been compared to thin wire antennas previously in [5], [6], [8]. However, the behavior of longitudinal-slots in the narrow wall of a rectangular waveguide that violate the condition in Equation 2.4 has not been studied.

The dimensions of the waveguide also affect the resonances of slot radiators. For narrow-wall longitudinal-slot, as the width of the slot increases, it can resonate for a longer or shorter length of slot as shown in Figure 2.4. The dimensions of the

waveguide used to obtain Figure 2.4 are the dimensions of standard S-band waveguide WR284, which is $72.14mm * 34.04mm$.

Consider a fixed operating frequency and the narrow dimension, b of the waveguide that is smaller than half the size of 'a'. The upper and lower limits of 'a', such that only the dominant (TE_{10}) mode propagates inside the waveguide, are determined as follows. The lower (upper) limit on the broad dimension is found from the cut-off frequency condition for the TE_{10} (TE_{20}) mode shown in Equation 2.11 (2.12). The resulting limits on the broad dimension of the waveguide are shown in Equation 2.13.

$$f_{c10} = \frac{1}{2\pi\sqrt{\mu_0\epsilon_0}}\frac{\pi}{a_1} \tag{2.11}$$

where:

a_1 is the lower limit on the borad dimension of the waveguide

μ_0 is the permeability of free space

ϵ_0 is the permittivity of free space

$$f_{c20} = \frac{1}{2\pi\sqrt{\mu_0\epsilon_0}}\frac{2\pi}{a_2} \tag{2.12}$$

where:

a_2 is the upper limit on the borad dimension of the waveguide

The value of a_1 (a_2) is found by solving Equation 2.11(2.12) after substituting 3.17GHz for the value of f_{c10} (f_{c20}).

$$47.3mm \ < \ a \ < \ 94.6mm \tag{2.13}$$

where:

a is the broad dimension of the waveguide

b is the narrow dimension of the waveguide and satisfies the condition $b \leq \frac{a}{2}$

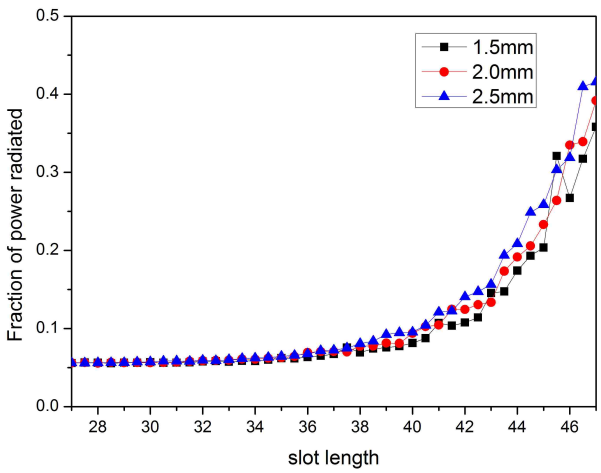

Figure 2.4: Resonances for a narrow-wall longitudinal-slot radiator. Each curve represents a specific slot width in mm.

Figures 2.5 through 2.9 also show some interesting properties of a narrow-wall longitudinal-slot. They show that irrespective of the dimensions of the slot, the amplitude/phase of the power transmitted/reflected by the slot through the waveguide and the phase of the induced aperture E-field at the center of the slot have a predictable dependence on the amplitude of the power radiated through the slot. The phase of the transmitted/reflected power through the waveguide is measured at the output/input port of the waveguide containing the shot. All the sampled phases are measured relative to the phase of the input power, which is equal to zero at the input port. Figures 2.5 through 2.9 are obtained from the data set, for which the length of the waveguide containing the slot is one guide wavelength long and the slot lengths (widths) ranged between 27mm (1.5mm) and 47mm (25mm).

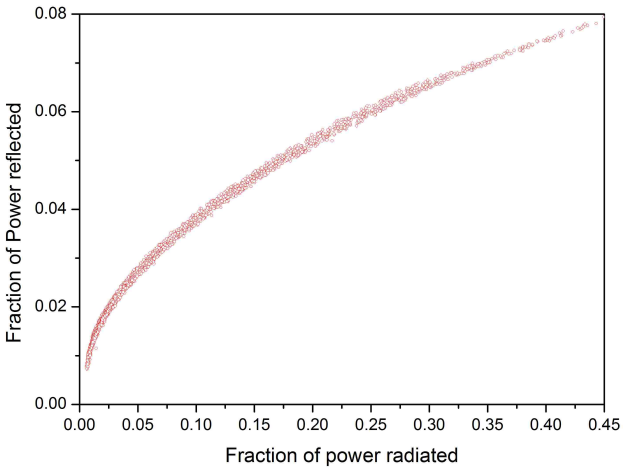

Figure 2.5: Relation between the amplitude of the power radiated through the slot and the power reflected through the waveguide of a narrow-wall longitudinal-slot.

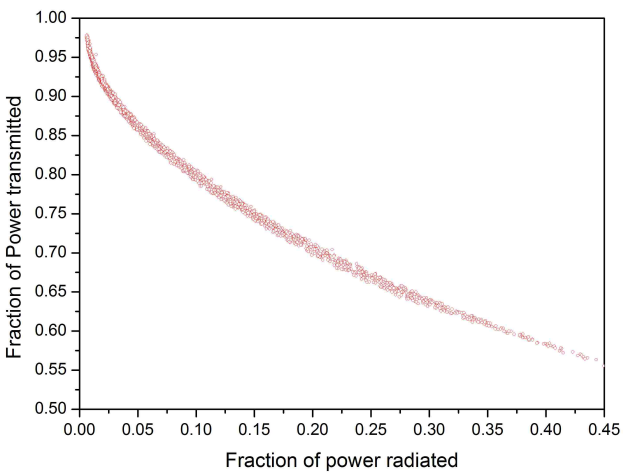

Figure 2.6: Relation between the amplitude of the power radiated through the slot and the power tansmitted through the waveguide of a narrow-wall longitudinal-slot.

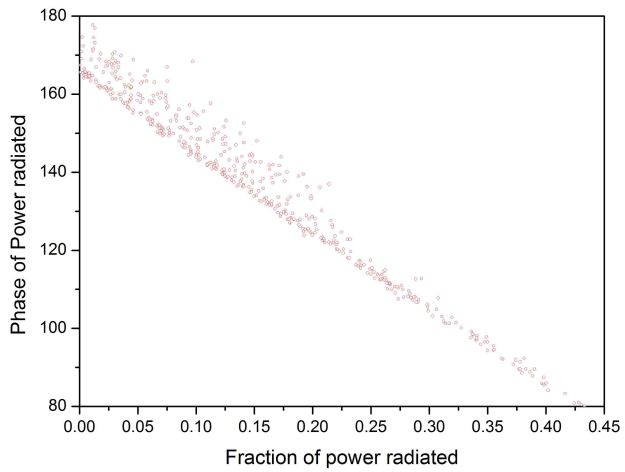

Figure 2.7: Relation between the amplitude of the power radiated through the slot and the phase of the power rradiated throught the slot.

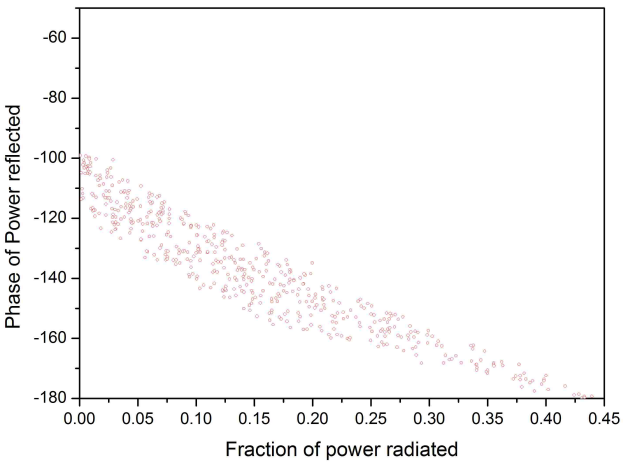

Figure 2.8: Relation between the amplitude of the power radiated through the slot and the phase of the power reflected through the waveguide of a narrow-wall longitudinal-slot.

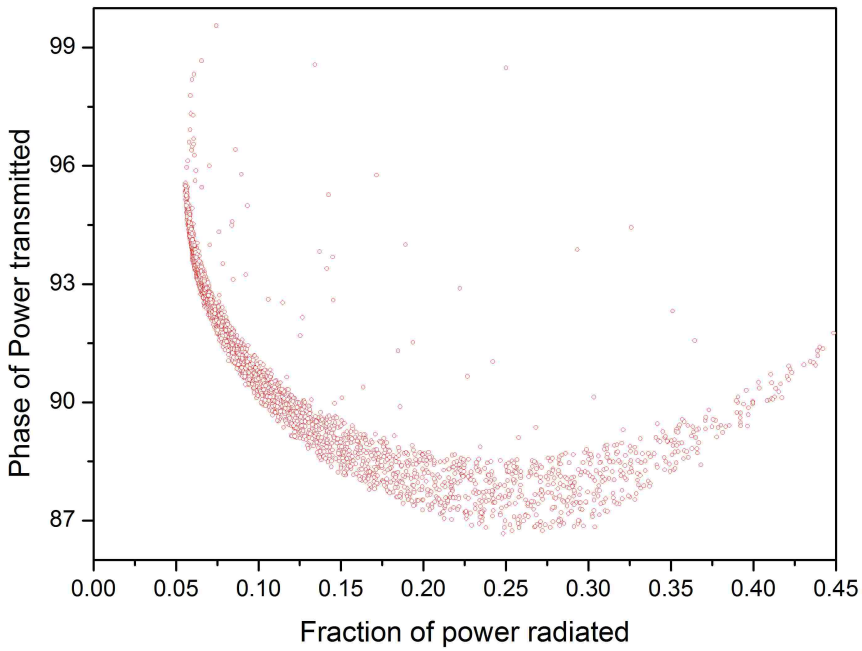

Figure 2.9: Relation between the amplitudes of the power radiated through the slot and the phase of power tansmitted through the waveguide ofr a narrow-wall longitudinal-slot.

2.2 S-band H-plane-bend radiator

The H-plane-bend-radiator (HPB-radiator) [1] is an H-plane bend terminating in a radiating aperture with the narrow dimension of the waveguide flaring out to the maximum possible width. The maximum possible width is the same as the maximum dimension for the narrow wall of a rectangular waveguide that still only supports the dominant (TE_{10}) mode. Figure 2.10 is a schematic of the HPB-radiator element to be used in the narrow-wall-slot-HPB-array described in Chapter 3. The design variables for the HPB-radiator are its aperture dimensions and the function

that determines the H-plane taper. The optimal HPB-radiator element has the same half sine wave aperture E-field distribution as a narrow-wall longitudinal-slot with minimal reflected power into the feed-waveguide.

The design of the HPB-radiator element with a smooth H-plane taper function using just analytical or computational electromagnetics techniques felt intractable. Thus, the design based on dimensional offset hypothesis [1] that process the computational analysis data using iterative search algorithms is proposed.

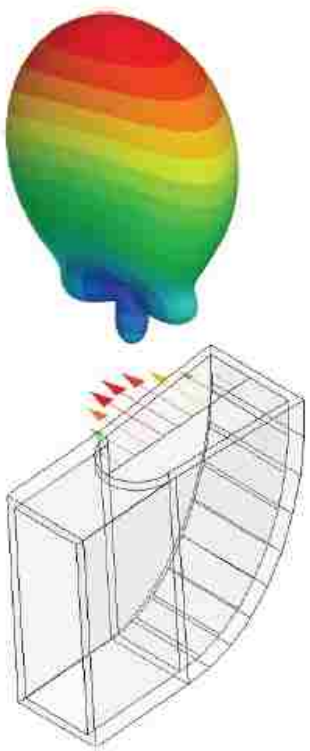

Figure 2.10: Narrow-wall-slot-HPB-array's HPB-radiator along with its aperture E-field distribution and the 3-D radiation power pattern in absolute units.

The HPB-radiator element, which is used as the last element in the narrow-wall-slot-HPB-array, is shown in Figure 2.10. It can be inferred from Chapter 3 that not only does the power reflected into the feed-waveguide by the HPB-radiator element

needs to be minimized, but also its aperture phase is critical in the performance of the narrow-wall longitudinal-slot array. The aperture length of the HPB-radiator greatly influences its aperture phase value that complements the narrow-wall longitudinal-slot array's performance. Specifically, an aperture length slightly greater than a half free space wavelength was found to be more suitable to produce a half-sine E-field distribution.

With respect to the HPB-radiator analysis in [1], the aperture of the HPB-radiator began at the same location along the length of the waveguide where the H-plane taper began. The length of the radiating aperture of the HPB-radiator was chosen to be a half free space wavelength. It is because of the fact that an aperture length greater than a half free space wavelength produces an aperture E-field that is not necessarily a half sine wave distribution for different taper functions, and on the other hand, a aperture length less than a half free space wavelength produced a higher reflected power into the feed-waveguide.

The design of the HPB-radiator element is therefore a best compromise between the reflected power into feeding waveguide, the aperture E-field distribution and the aperture phase. This was achieved by naga [1] for the design shown in Figure 2.10. The aperture of the HPB-radiator begins at a location along the length of the waveguide that is approximately 12.6mm before the beginning of the H-plane taper, and the length of the aperture is approximately 60mm, where 47.4mm corresponds to a half free space wavelength at 3.17GHz. The taper function used for the HPB-radiator in Figure 2.10 is defined by the equation of an ellipse.

For this best compromise design: the power reflected into the feed-waveguide is less than 1%, with an approximately half sine wave aperture E-field distribution. The aperture phase also complements the performance of the narrow-wall longitudinal-slot array as will be shown in Chapter 3.

Chapter 3

Narrow-wall Longitudinal-slot array with HPB-radiator

An illustration of the narrow-wall longitudinal-slot array with an HPB-radiator element is shown in Figure 3.1. This single array antenna is designed to maximize the directivity of its main lobe and to minimize the reflected power into its feed-waveguide. The design presented by Baum [2] is considered. The center-to-center distance between any two adjacent array elements is kept the same. The last element of the array, i.e. the HPB-radiator, has been described and analyzed in Chapter 2. As mentioned in Chapter 1, the dimensions of the slots considered in this array's design satisfied the condition given by Equation 2.10. Under this condition, all the slots produced a very similar half sine wave aperture E-field distribution. To maximize the peak directivity of the array, the elements of the array are designed to radiated equal powers and possess a constant progressive phase shift so that the design forms a uniform array. In order to minimize the power reflected into the feed-waveguide, the power reflected into individual elements need to be destructively interfering. The optimal single-array design is a tradeoff between minimizing the reflected power at the input of the array and designing a perfect uniform array.

The number of elements in the single array was restricted to five and the maximum allowable inter-elemnet spacing was restricted to one guide wavelength, so that the S-band antenna is front mountable on a land vehicle.

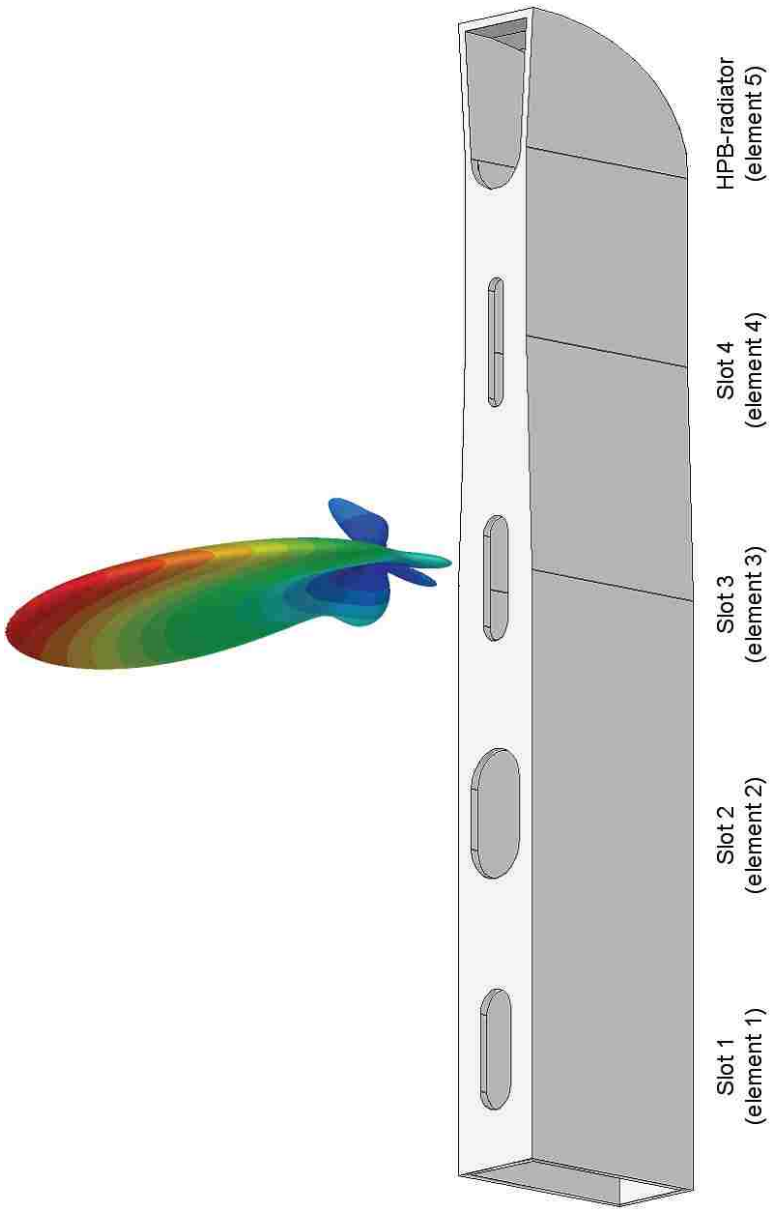

Figure 3.1: Narrow-slot-HPB-array along with its 3-D radiation power pattern in absolute units.

3.1 Microwave Network Analysis

The narrow-wall-slot-HPB-array is designed by optimizing the mutual coupling through the waveguide between the array elements given the design variables and criterias, which are the slots' dimensions, spacing between the elements and the narrow-wall taper. In this analysis, the external coupling between the array elements is ignored and the mutual coupling analysis is performed using microwave network theory. Each radiating slot is considered as a lossy two-port network, where the loss represents the power radiated by the slot; the HPB-radiator is represented as a lossy one-port network. The S-parameters and aperture phases of the array elements are obtained from computational analysis performed by HFSS, which was presented in Chapter 2. Figure 3.2 shows the array in Figure 3.1 equivalent to a microwave network. $P_{in(n)}$ are the powers being input at the input ports to the nth lossy network (n from 1 to 5). $P_{rad(n)}$ are the powers radiated by the elements through 1 to 5. Γ_n are the reflection coefficients.

Besides the reason for the reflected power to be minimized so as to maximize antenna gain and protect the high power microwave source, an additional reason is as follows. There is high possibility that the radiation pattern of the narrow-wall-slot-HPB-array would have its main lobe canted from the broadside direction, it is advantageous to have power flow in only one direction along the length of the linear array, as the goal of this design is to maximize the directivity,

Although the powers radiated by all the elements need to be equal, the fractions of the power radiated by the slots to the amount of power being input to the corresponding elements are different from each other. For instance, the ideal case is that when Γ_1 through Γ_5 are equal to zero, the optimal values for P_{rad1} through P_{rad5} are given by $0.2P_{in1}$, $2.5P_{in2}$, $P_{in3}/3$, $0.5P_{in4}$, P_{in5} respectively.

Since in reality Γ_1 through Γ_5 are not equal to zero, the goal of the microwave

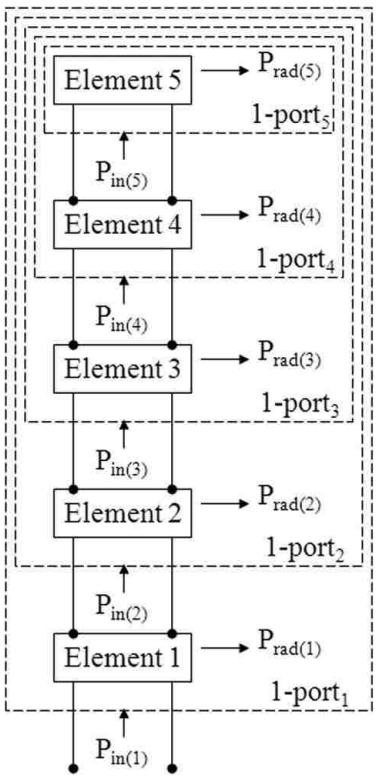

Figure 3.2: Equivalent microwave network of the narrow-wall-slot-HPB-array.

network analysis is to obtain expression for Γ_1, P_{rad1} through P_{rad5} in terms of P_{in1}, the S-parameters of the element 1 through 5, and the distance between the array elements. The effect of mutual coupling on the aperture phases obtained from computational analysis of the array elements 1 through 5, is factored in by simply knowing the distance between the elements and the phase of the input powers P_{in1} through P_{in5}. Hence, the aperture phase of slot 1 is only influenced by the phase of P_{in1} and the location of the array's input port from slot 1. Similarly, the aperture phase of slot 2 is only influenced by the phase of P_{in2} and the distance between slot 1 and slot 2. This aperture phase calculation procedure can be extended to the other elements. Note that the aperture phase calculations assume that the Γ s are designed small enough and therefore do not affect the calculations.

We start the microwave network analysis by beginning at the HPB-radiator element and moving towards the input of the array, one element at a time, until slot 1 is reached; then by moving from slot 1 towards the end of the array, one element at a time, until the HPB-radiator is reached, thus completes the analysis. The goal of the reverse (forward) path analysis is to obtain the expressions for Γ_1, P_{rad1} through P_{rad5} in terms of P_{in1}, the S-parameters of the array element 1 through 5, and the distance between the array elements.

The inter-element spacing between the array elements can be treated as a phase shift in the S-parameters of the individual elements. This can be achieved by a shift in reference planes', and is discussed in detail in [10].

The first step of the analysis is illustrated in Figure 3.3. 'Load 5' in Figure 3.3 represents the array element 5. V_1^+, V_2^+, V_1^-, V_1^- in Figure 4.4 represent the voltage waves are known in the microwave network analysis performed using S-parameters. Following standard S-parameter network analysis, the network shown in Figure 3.3 satisfies Equation 3.1, 3.2 and 3.3; S_{11}, S_{12}, S_{21}, S_{22} represent the S-parameters of the two-port network which represents slot 4; Γ_5 is the reflection coefficient of the one-port lossy network (Load 5) that represents the HPB-radiator.

$$V_2^+ = \Gamma_5 V_2^- \tag{3.1}$$

$$V_2^- = S_{21} V_1^+ + S_{22} V_2^+ \tag{3.2}$$

$$V_1^- = S_{11} V_1^+ + S_{12} V_2^+ \tag{3.3}$$

Equation 3.1, 3.2, 3.2 can be solved to obtain the expressions in Equation 3.4 through 3.10. The reflection coefficient shown in Equation 3.6, while port 1 of the network in Figure 3.3 is matched, is calculated and recorded to be used in the following step of the analysis.

$$\frac{V_2^-}{V_1^+} = \frac{S_{21}}{1 - \Gamma_5 S_{22}} \tag{3.4}$$

$$\frac{V_2^+}{V_1^-} = \frac{\Gamma_5 S_{21}}{1 - \Gamma_5 S_{22}} \tag{3.5}$$

$$\Gamma_4 = \frac{V_1^-}{V_1^+} = S_{11} + \Gamma_5 S_{12} \frac{V_2^-}{V^+} \tag{3.6}$$

$$P_{in5} = P_{in4} \left| \frac{V_2^-}{V_1^+} \right|^2 \tag{3.7}$$

$$P_{ref4} = P_{in4} \left| \Gamma_4 \right|^2 \tag{3.8}$$

$$P_{load5} = P_{in4} \left(\left| \frac{V_2^-}{V_1^+} \right|^2 - \left| \frac{V_2^+}{V_1^+} \right|^2 \right) \tag{3.9}$$

$$P_{rad4} = P_{in4} - P_{ref4} - P_{load5} \tag{3.10}$$

where:

P_{in4} is the power being input at port 1 of the two-port network that represents slot 4 in Figure 3.3

P_{ref4} is the power reflected at port 1 in Figure 3.3 under matched port conditions

P_{load5} is the power delivered to the HPB-radiator

P_{rad4} is the power radiated by slot 4

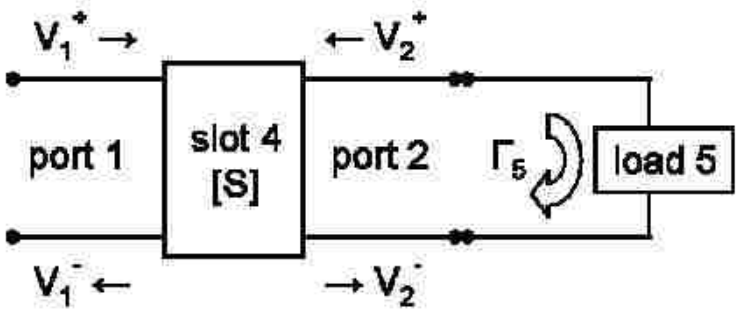

Figure 3.3: Illustration for the first step in the path analysis.

In the second step of the analysis, the complete network in Figure 3.3 is considered as a one-port network (labeled as 'load 4' in Figure 3.4) with Γ_4 computed in Equation 3.5 representing its reflection coefficient. This one-port network is now connected to equivalent two-port network for slot 3 as shown in Figure 3.4. Similar to previous analysis, the analysis of this two-port network connected to the one-port network continues. In addition, the power reflected at port 1 in Figure 3.4 (P_{ref3}), the power delivered to load 4 (P_{load4}) and the power radiated by slot 3 (P_{rad3}) are obtained in terms of the power being input at port 1 of the two-port network that represents slot 3 in Figure 3.4 (P_{in3}). This analysis procedure is complete when it reached the first element, at which point, the value of the effective reflection coefficient at the input of the complete network as shown in Figure 3.2 (Γ_1) is found.

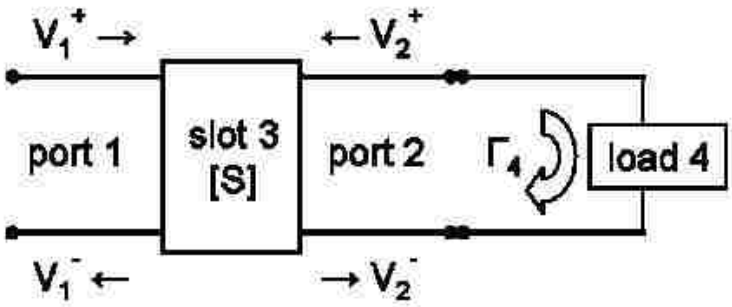

Figure 3.4: Illustration for the second step in the path analysis.

The analysis continues with a series of steps similar to reverse path analysis and the first step is illustrated in Figure 3.5. 'Load 2' in Figure 3.5 represents array elements 2 through 5. Hence, it can be inferred that by starting from a known value for P_{in1}, the values for P_{rad1} and P_{in2} can be found. The second step is illustrated in Figure 3.6. 'load 3' in Figure 3.6 represents array elements 3 through 5. From the value of P_{in2} obtained from the previous step, the values of P_{rad2} and P_{in3} can be found. This analysis continues until it eventually find all the powers radiated by the array elements, P_{rad1} through P_{rad5}.

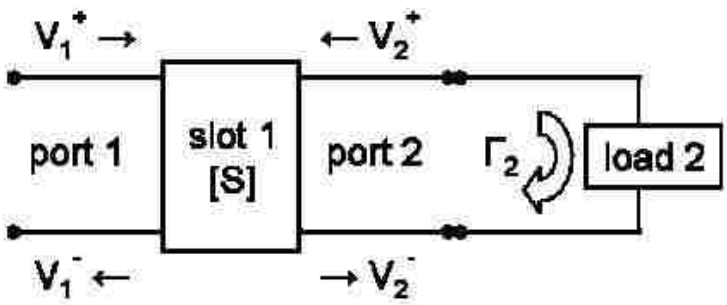

Figure 3.5: Illustration for the first step in the forward path analysis.

The S-parameters and aperture phases of the individual array elements are obtained from HFSS simulations. The inputs to the routine were the S-parameters and aperture phases of slots with lengths (widths) varying between 44mm (1.5m-

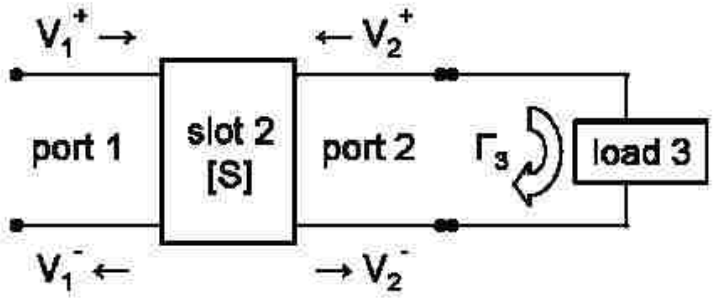

Figure 3.6: Illustration for the second step in the forward path analysis.

Table 3.1: The optimal dimensions of the slots.

slot 1	slot 2	slot 3	slot 4
$44.2mm * 15.8mm$	$47.3mm * 25.2mm$	$45.8mm * 12.6mm$	$47.3mm * 7.9mm$

m) and 47.5mm (25.5mm), and the S-parameter and aperture phase of the optimal HPB-radiator element for the narrow-wall-slot-HPB-array presented in Chapter 2.

The optimal values obtained from the MATLAB routine for the reflected power, mean error in the progressive phase shift, mean offset between the radiated powers are: $< 1\%$, 3.7^o, 1.2% respectively. The optimal spacing between the slots was $11\lambda_g/16$, where λ_g is the guide wavelength for an S-band waveguide operating at 3.17GHz. Table 3.1 shows the optimal dimensions for slot 1 through slot 4.

3.2 Full wave analysis of narrow-wall-slot-HPB-array

As mentioned before, the external coupling between array elements is neglected in the previous microwave network analysis. The slot array is also simulated in HFSS using the optimal dimensions for the slot obtained from the MATLAB routine, so as

Table 3.2: Results from microwave network analysi and full-wave analysis.

	Full-wave analysis		Microwave network analysis	
element	power radiated	aperture phase	power radiated	aperture phase
slot 1	20.3%	207.7^o	19.8%	194.4^o
slot 2	20.2%	294.7^o	19.6%	287.7^o
slot 3	19.8%	38.0^o	19.8%	22.1^o
slot 4	17.3%	114^o	17.5%	106.7^o
HPB radiator	22.4%	249^o	22.9%	209.0^o

to include external coupling in the antenna analysis. The reflected power at the input of the array is $< 1\%$. Table 3.2 compares the values of power radiated and aperture phases of the array element 1 through 5 obtained from the full-wave analysis with the optimized results from microwave network analysis. Table 3.2 shows that there is good agreement between the microwave network analysis result and the full-wave analysis result.

In HFSS simulations, there is a narrow-wall flare [1] introduced near the array element 4, which is the last slot next to the HPB-radiator, as shown in Figure 3.7, where the narrow dimension of the waveguide is squeezed by 20 % to increase the radiated power through slot 4. Figure 3.7 shows the slot array along with its 3-D absolute antenna gain in dimensionless units. Figure 3.9 shows the H-plane radiation power patterns of the slot array; $\theta = 0^o$ on the horizontal axis of the plot in Figure 3.8 corresponds to the broadside direction.

Figure 3.9 presents the radiation power patterns of the narrow-wall-slot-array in the plane cut that is orthogonal to the H-plane, and passing through the $\theta = -15^o$ line shown in Figure 3.8; $\phi = 0^o$ on the horizontal axis of the plot in Figure 3.9 corresponds to the same point in the 3-D radiation power pattern as $\theta = -15^o$ on the horizontal axis of the plot in Figure 3.8.

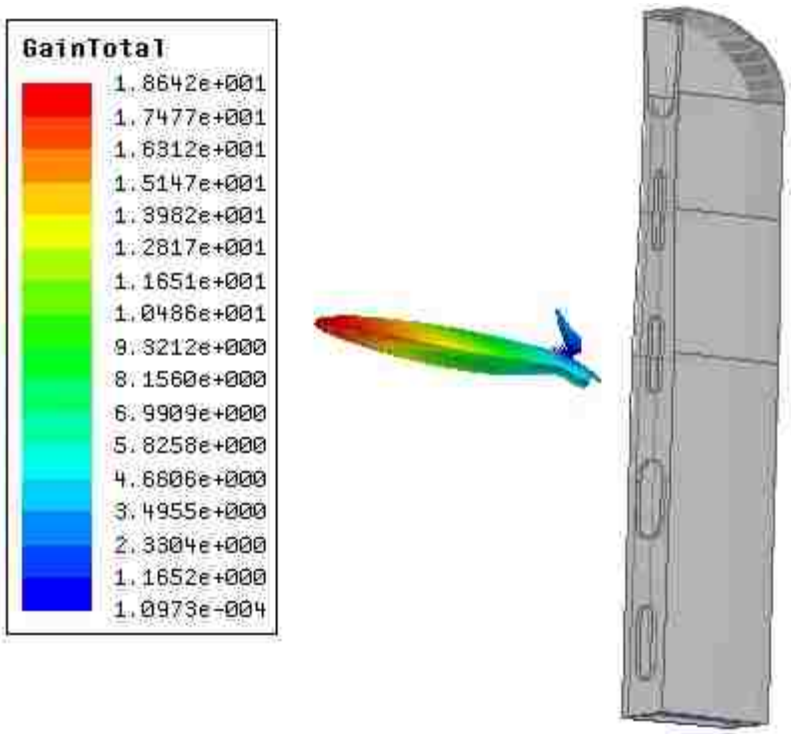

Figure 3.7: slot array along with its 3-D absolute antenna gain in dimensionless units.

3.3 Power handling ability

The power handling capability analysis for the array design in the S band is done with the aid of HFSS. Full-wave analysis is performed on the array designs at 3.17 GHz. The magnitudes of the E-field values inside the structures are obtained and the maximum field values are recorded. The well-known electrical air breakdown value of approximately 3MV/m [11] for static fields at one atmosphere of air pressure is used as the upper limit for the maximum allowable E-field values inside the structures. So, for the narrow-wall longitudinal-slot array operating at 3.17 GHz, at the air pressure of one atmosphere, an input power of approximately 1.65MW through the S-band feed-waveguide produced air breakdown inside the structure.

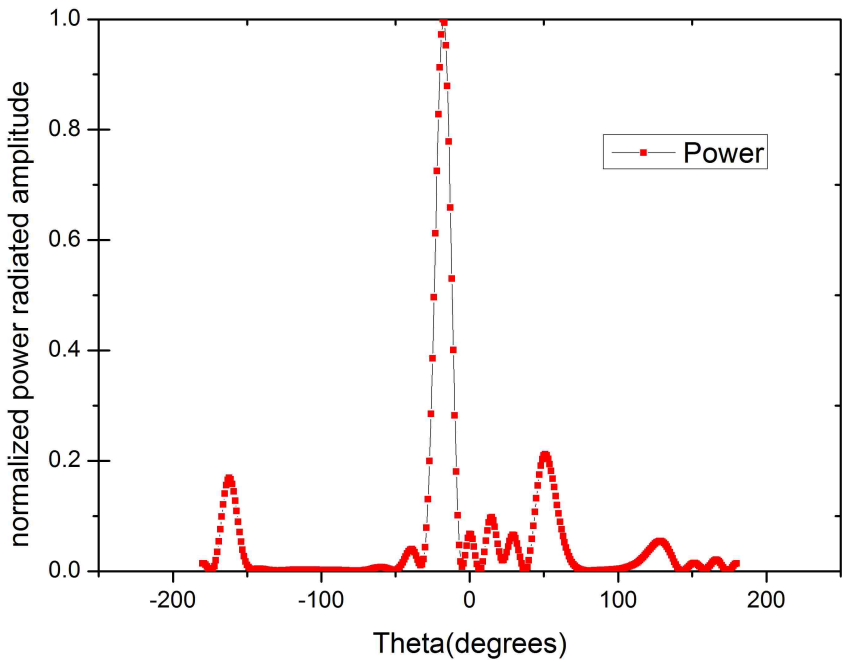

Figure 3.8: H-plane radiation power pattern of the slot array.

The air pressure at sea level is approximately one atmosphere, i.e. 760Torr. When antennas are operating at increasing altitudes above sea level, the value of air pressure falls, consequently, the electrical air breakdown values also falls[12]. Therefore, the maximum allowable power through the S-band feed-waveguide needs to be adjusted depending on the altitude of the antennas operating at.

The pressure at an elevation of 'h' meters above sea level can be computed using Equation 3.11.

$$p(h) = p(0)e^{-(\frac{h}{H})} \tag{3.11}$$

where:

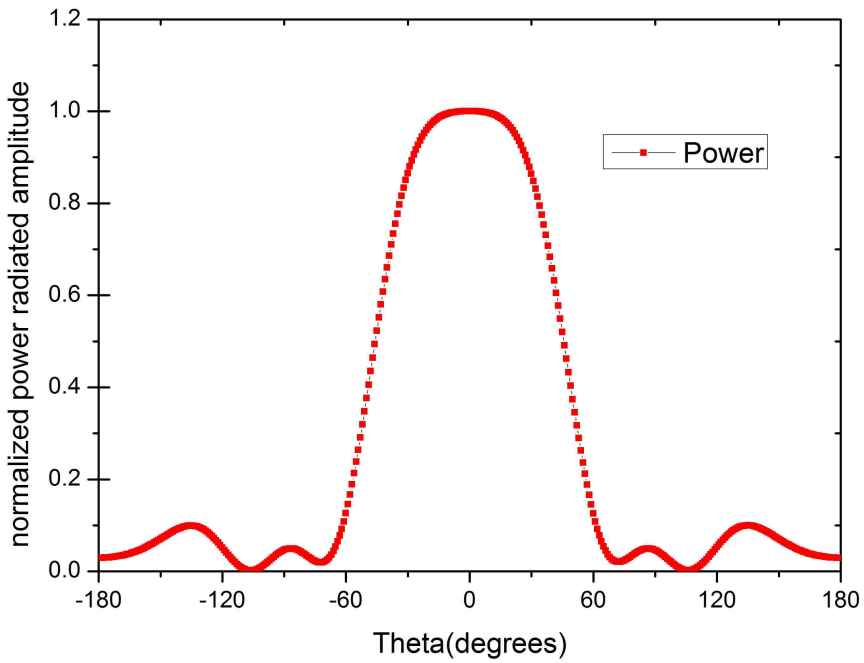

Figure 3.9: Radiation power pattern in the plane cut that is orthogonal to the H-plane and passing through the $\theta = -15^o$ line shown in Figure 3.8 of the slot array.

$p(h)$ is the air pressure at an elevation of 'h' meters above sea level

$p(0)$ (=760 Torr) is the air pressure at sea level

H (=8400 meters) is the approximate scale height of the Earth's atmosphere

Between the air pressure values of 260 Torr and 760 Torr, the electrical air breakdown are directly proportional to the air pressure values, and can be computed through Equation 3.12.

$$E\_field\_Br = \frac{(p)(E\_field\_Br_0)}{p_0} \tag{3.12}$$

where:

$p(0)$ (=760 Torr) is the air pressure at sea level

$E\_field\_Br_0$ (=3MV/m) is the breakdown E-field value for static fields at one atmosphere air pressure

p is the value of air pressure between the values of 260 Torr and 760 Torr

$E\_field\_Br_0$ is the breakdown E-field value for static fields at an air pressure of 'p'

It is now illustrated how the power handling capability of a high power antenna is affected by the operating location. Consider, for instance, that the antenna operates in Albuquerque, New Mexico, U.S.A. at an elevation of approximately 1610 meters above sea level. From Equation 3.11, the air pressure in Albuquerque is approximately equal to 627.44 Torr. And this air pressure is in the range of air pressure values mentioned before for which Equation 3.12 is valid. The corresponding air breakdown value in Albuquerque is computed from Equation 3.12 and is approximately equal to 2.48MV/m.

As a result, for the narrow-wall longitudinal-slot array operating at 3.17 GHz in Albuquerque, New Mexico, U.S.A., an input power of approximately 1.15MW through the S-band feed-waveguide would produce air breakdown inside the structure. This is approximately 70% of the amount of power that the corresponding array can handle at one atmosphere of air pressure.

Chapter 4

Additional Designs of Narrow-wall Longitudinal-slot array

A couple of additional designs are given in this section. Among all these designs based on narrow-wall longitudinal-slot array, the best antenna design is the double-narrow-wall-slot-array. From the previous section, we know that the peak gain for the optimized narrow-wall longitudinal-slot array is approximately 12.5dB. The double-narrow-wall-slot-array design can increase this peak gain to approximately 14.9dB. The curved-narrow-wall-slot-array design is to perform as a conformal antenna structure and circularly polarized narrow-wall slot-array is designed to produce both vertically and horizontally polarized radiated power. The study of the capability of beam-steering is also conducted

4.1 Double-narrow-wall-slot-array

As mentioned above, in order to increase the peak gain of the optimized narrow-wall longitudinal-slot array, the double array, as shown in Figure 4.1, was proposed

by Baum [2]. This double array consists of two identical slot arrays with a common wall; the slots are moved as close to the common wall as possible, with the apertures of one slot array alternating those of the other. The center-to-center distance is kept constant and the input phase of one array is also shifted from the other so as to ensure that the aperture phases of the slots in double array have an approximately constant phase progression.

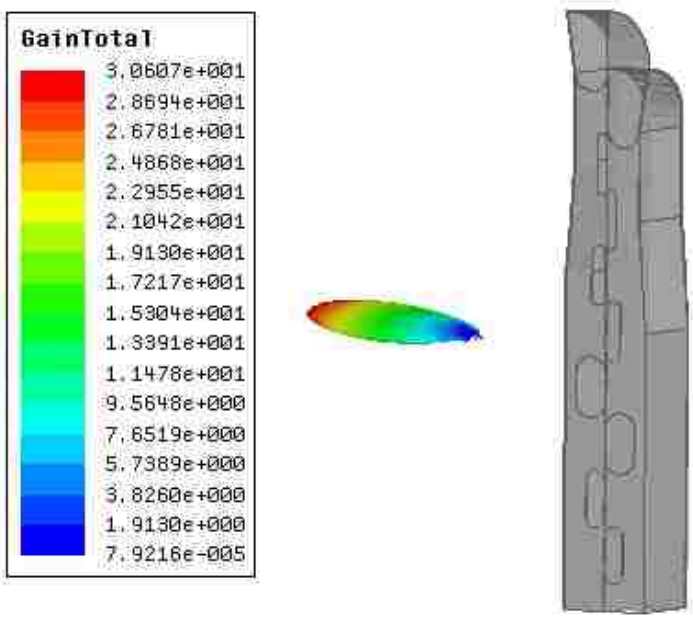

Figure 4.1: Double-narrow-wall-slot-array with its 3-D absolute gain in dimensionless units.

The double-narrow-wall-slot-array has approximately the same length as the single array, but by increasing the number of elements in the array with an approximately constant favorable phase progression, a higher peak gain is achieved. In other words, the aperture filed distribution of the double array is much more uniform than that of the single array, thereby resulting in a higher gain.

This proposed configuration has comparable inter-element spacing (d) and aver-

age progressive phase shift (β). According to Equation 4.1 by balanis [9], we can find the array factor for the double array.

$$AF = \frac{sin\ (\frac{N}{2}(2\pi\frac{d}{\lambda}sin(\theta)+\beta))}{sin\ (\frac{1}{2}\ (2\pi\frac{d}{\lambda}sin(\theta)+\beta))} \tag{4.1}$$

Where:

N is the number of array elements

d is the inter-element spacing

θ is the observation angle, where $\theta = 0^o$ corresponds to the broadside direction of the array.

β is the progressive phase shif and is expressed as a positive number

The array factor in Equation 4.1 is maximized when the condition in Equation 4.2 is satisfied. Equation 4.3 gives the directions in which the array factor achieves its maxima, where θ_o corresponds to the direction of the main lobe and θ_1, θ_2,... correspond to the directions of the side lobes.

$$\frac{1}{2}\ (2\pi\frac{d}{\lambda}sin(\theta)+\beta) = m\pi \tag{4.2}$$

where:

m =0,1,2,...

$$\theta_m = sin^{-1}\ (\frac{1}{2\pi(d/\lambda)}(-\beta+2m\pi)) \tag{4.3}$$

From previous analysis, we know that the optimal inter-element spacing (d) and average progressive phase shift (β) of single array are approximately 0.91λ and 93.7^o, where λ is the free space wavelength. From Equation 4.9, the values of $m = 0$ and $m = 1$ return real values for θ_m. These values of θ_0 and θ_1 are approximately -16^o

and 54^o, respectively.

$$2\pi\frac{d}{\lambda} \; < \; -\beta + 2\pi \tag{4.4}$$

Equation 4.4 is obtained from Equation 4.3, which gives the condition for avoiding grating lobes. The elements of the double array are properly organized such that Equation 4.4 is satisfied. Hence the double array has a maximum side lobe level of approximately -10.7dB compared to that of the single array of -7.2dB, while maintaining the directive main beam as shown in Figure 4.2 and Figure 4.3.

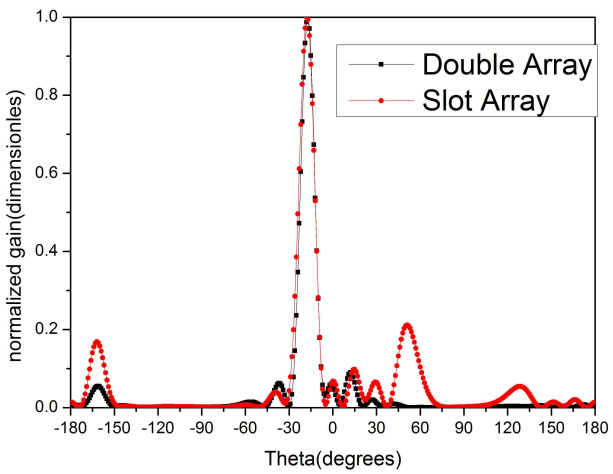

Figure 4.2: H-plane radiation power patterns of the slot array and the double array.

4.2 Curved-narrow-wall-slot-array

This high-power antenna can be designed to be front mounted on land vehicles. Taking into account the varying shapes of vehicles, a curved-narrow-wall-slot array design was developed as a conformal antenna structure. The narrow wall of the waveguide was bent based on an elliptical curve. As shown in Figure 4.4, the direction

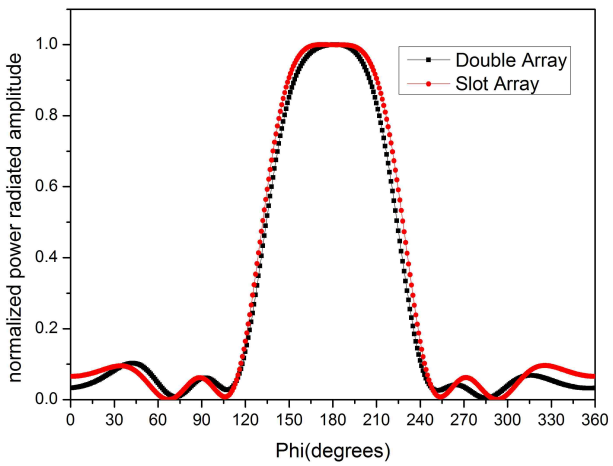

Figure 4.3: Radiation power patterns of the slot array and the double array in the plane cut orthogonal to the H-plane and passing through the $\theta = -15^o$ line shown in Figure 4.2.

of the wave propagating in the waveguide is along the transverse diameter of the elliptical curve and the narrow side of the waveguide is along the conjugate diameter of the elliptical curve.

The idea of bending the waveguide is done by placing the five elements of the uniform array on the curved surface, keeping the distance and progressive phase shift between these five elements as close as possible to the parameters of the straight waveguide slot array design.

Due to the bend of the waveguide antenna, the small distances among those five elements along the narrow side of the waveguide aperture will affect the total gain of the array. It is obvious that if the center of the third element is set to be the center of the coordinate system, the other four elements on the curved surface are required to have compensating phase to account for the varying path lengths of the radio waves due to the nonlinear locations of individual elements.

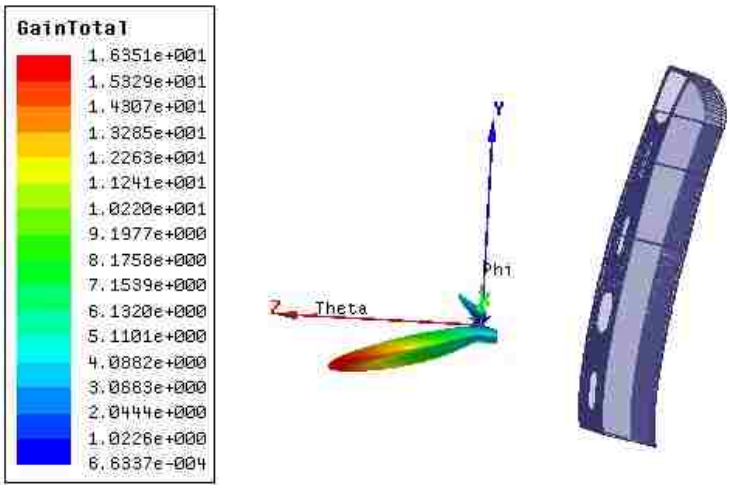

Figure 4.4: Curved-narrow-wall-slot-array with its 3-D absolute gain in dimensionless units.

With the help of HFSS, the curved narrow wall slot array was analyzed. Figure 4.5 presents the comparison between the H-plane radiation pattern of the curved

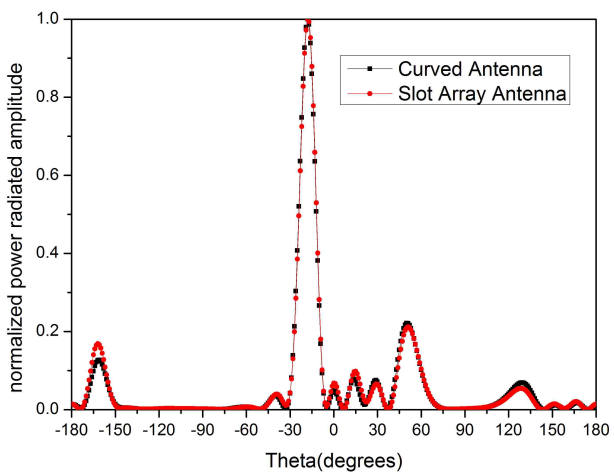

Figure 4.5: H-plane radiation power patterns of the slot array and the curved antenna.

narrow wall slot array and the narrow-wall longitudinal-slot array. Figure 4.6 shows

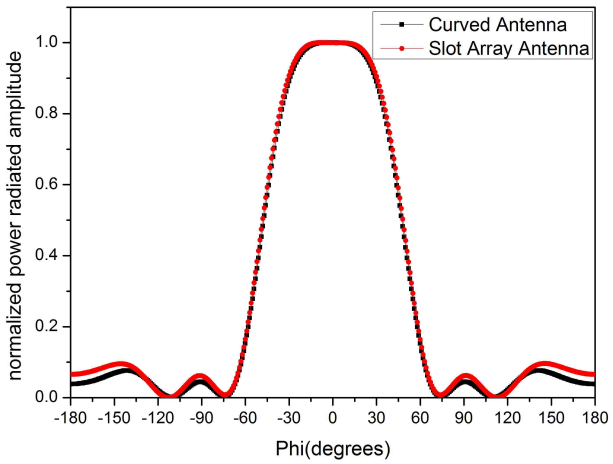

Figure 4.6: Radiation power patterns of the slot array and the curved antenna in the plane cut orthogonal to the H-plane and passing through the $\theta = -15^o$ line shown in Figure 4.5.

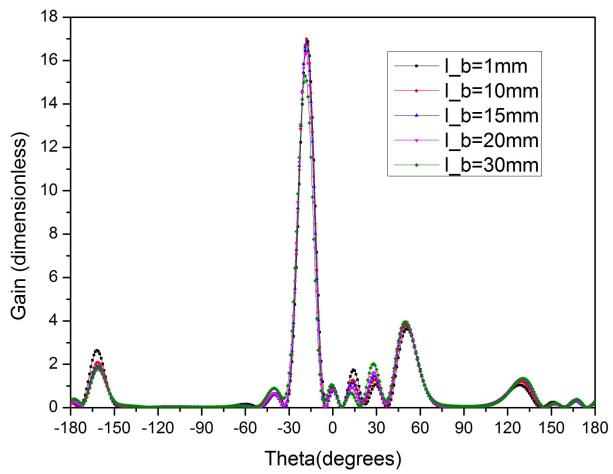

Figure 4.7: The relation between the radiation pattern and the curvature of the curved antenna

the radiation power pattern of the slot array and the curved antenna in the plane cut orthogonal to the H-plane and passing through the $\theta = -15^o$ line shown in Figure 4.4.

Figure 4.7 presents the relation between the radiation pattern and the curvature of the curved antenna. The more the antenna is bent, the less peak gain the antenna gets. In the figure, l_b represents the conjugate diameter of the ellipse which the curved surface is based on and the transverse diameter is fixed at $220mm$.

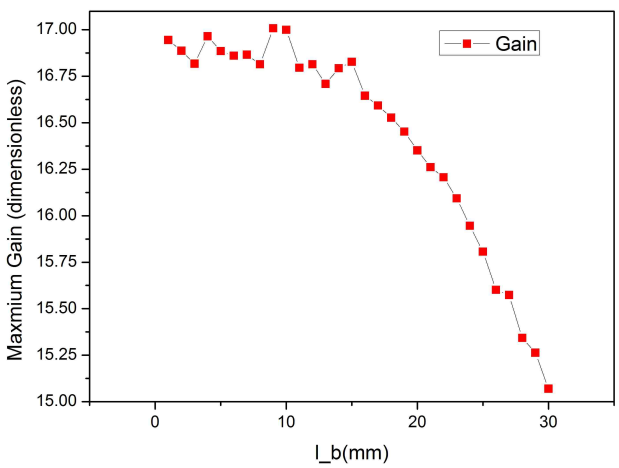

Figure 4.8: The relation between the maximum gain of the curved antenna and the curvature of the curved antenna.

Figure 4.8 presents the relation between the maximum gain of the curved antenna and the curvature of the curved antenna. Again, l_b represents the conjugate diameter of the ellipse which the curved antenna is based on and the transverse diameter is fixed at $220mm$.

The results obtained from HFSS verify our assumption that the uniform array will be maintained but the maximum gain will be decreased because of the curved structure applied to the narrow-wall longitudinal-slot array design.

4.3 Circularly-polarized Narrow-wall slot-array

All the above antenna designs produce the same horizontal polarization as the structure in Figure 1.1. This structure is required to produce vertically as well as horizontally polarized radiation. A couple of options for developing a single high power waveguide antenna that radiates circularly polarized power are shown in Figure 4.9, 4.10 and 4.11.

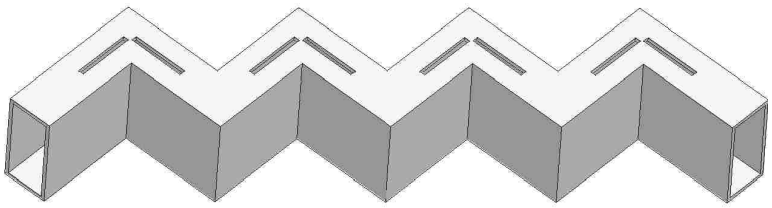

Figure 4.9: Circularly polarized slot array.

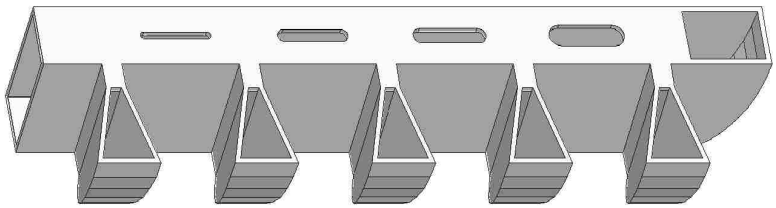

Figure 4.10: Circularly polarized slot array.

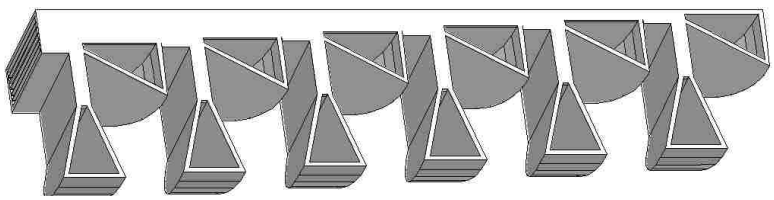

Figure 4.11: Circularly polarized slot array.

Some existing waveguide antenna that produce circularly polarized radiated fields can be found in [13] [14]. But the structures shown in Figure 4.9, 4.10 and 4.11 are

better suited for high power applications. The bends in Figure 4.9, 4.10 and 4.11 can be optimized for minimum reflections using the same techniques that were used to design the HPB-radiator's H-plane taper. The advantage of the circular-polarized-slot array design is its structural simplicity, consdering the need for two high power antennas to radiate both vertically and horizontally polarzied power.

To verify the realizability of the circularly polarized slot array antenna, we simulated the structure in Figure 4.9 in HFSS. We applied the narrow-wall longitudinal-slot array to the structure in Figure 4.1 by replacing the HPB-radiator with a matched port so that all the power into the port will be absorbed instead of being reflected. And the length of the narrow-wall longitudinal-radiator is set to be $5/8\lambda_g$ instead of $11/16\lambda_g$. Therefore, we established a two element array, of which each element consists of two narrow-wall longitudinal-slot radiators placed orthogonal to each other and with a phase shift of approximately 90^o at the center of the slots. Figure 4.12 shows the 3-D radiation pattern of this structure. Since it's a two element array, it is inevitable to have side lobes as shown in Figure 4.12. Figure 4.13

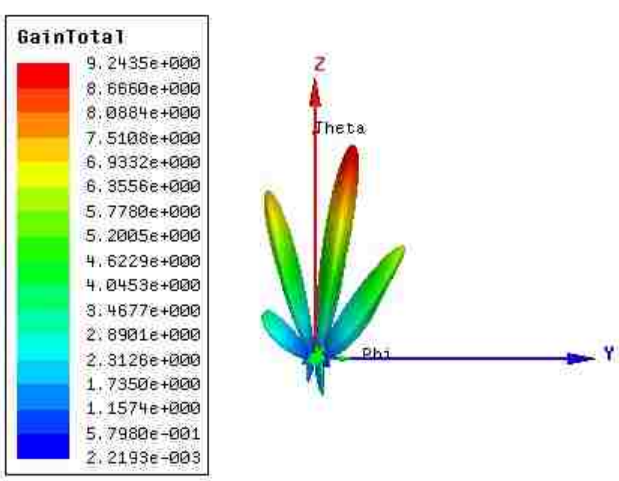

Figure 4.12: 3D radiation pattern of Circularly-polarized slot array.

presents the axial ratio of the antenna on the plane cut orthogonal to H-plane and

passing through $\theta = -6^o$ line, which corresponds to the direction of the maximum beam.

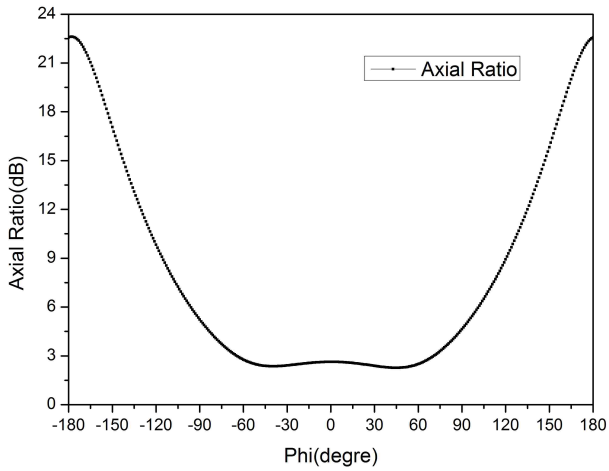

Figure 4.13: Axial ratio of the antenna on the plane cut orthogonal to H-plane and passing through $\theta = -6^o$ line.

From Figure 4.13, we obtain that in the range from $\phi = -60^o$ to $\phi = 60^o$ the axial ratio is less than 3dB. This range corresponds to the main beam on the plane cut orthogonal to H-plane. Hence, we conclude that the structure in Figure 4.9 is applicable. However, to realize circularly polarized antennas for high power applications, the array has to be redesigned to surpress side lobes in Figure 4.12. That is to say that the number of elements of the array needs to be increased.

4.4 Study of beam-steering capability

The antenna can be designed to be front mountable on land vehicles. In this section, we will study the capability of beam steering of this narrow-wall longitudinal-slot-array antenna.

4.4.1 H-plane Beam-steering

We start with H-plane radiation pattern from Figure 3.8 and we know the expression for the array factor of the narrow-wall longitudinal-slot array from Equation 4.1. In order to accomplish beam steering in the H-plane of the antenna, it requires that either the distance between adjacent elements or the progressive phase shift to vary.

However, in the design of the narrow-wall longitudinal-slots array, it is obvious that the progressive phase shift is related to the distance between adjacent elements of the uniform array. Thus, we varied the distance d from $0.5\lambda_g$ to λ_g (λ_g is the guide wavelength at 3.17GHz)in HFSS simulation, presented in Figure 4.14.

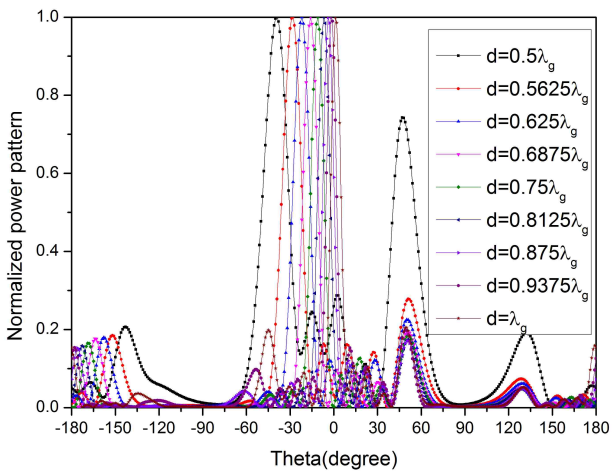

Figure 4.14: H-plane radiation pattern for different element distance d.

How can we realize these changes of distance d considering that the design is based on a air-filled metal rectangular waveguide?

We established a mechanism as presented in Figure 4.15. We put 4 copper patches symmetrically over those slots. By moving the patches towards the center of the

array. l1 in Figure 4.16 corresponds to the distance that the innner pair of the patches move. The distance between elements becomes $d - l1/2$ while the outer pair of the patches move a distance of $2l1$.

Figure 4.15: Beamsteering mechanism of the narrow-wall longitudinal-slot array.

This mechanism is simulated in HFSS, and Figure 4.16 shows the H-plane radiation pattern corresponding to various values of l_1. It turns out the main beam of the H-plane radiation pattern moved between $\theta = -15^o$ and $\theta = -20^o$.

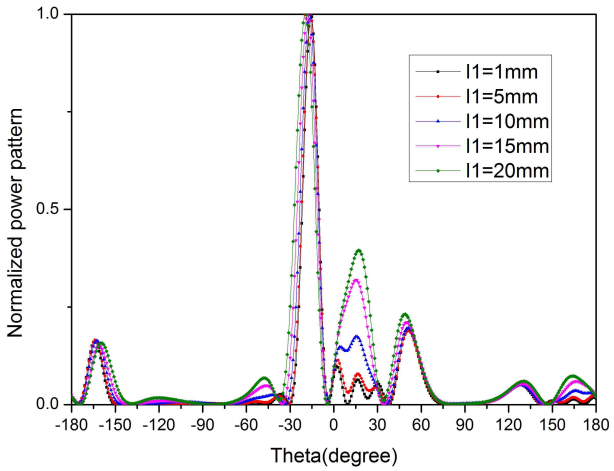

Figure 4.16: Beamsteering mechanism of the narrow-wall longitudinal-slot array.

Similarly, we established another mechanism as presented in Figure 4.17. We put 4 copper patches symmetrically over those slots. By moving the patches away from the center of the array. l1 in Figure 4.18 corresponds to the distance that the innner pair of the patches move. The distance between elements becomes $d+l1/2$ while the outer pair of the patches move a distance of $2l1$.

Figure 4.17: H-plane normalized Radiation pattern under the beamsteering mechanism of the narrow-wall longitudinal-slot array.

Figure 4.18 shows the H-plane radiation pattern corresponding to various values of l_1. This figure uses power pattern in dimensionless units instead of normalized power pattern to better illustrate that the main beam of H-plane radiation pattern does not move as the copper patches move.

From the above discussion, we conclude that the narrow-wall longitudinal-slot array can achieve beam steering as shown in Figure 4.10, by decreasing the distance between the elements of the uniform array designed in Chapter 3. As a result, the main beam moves from $\theta = -15^o$ to $\theta = -20^o$. And it turns out that similar mechanism proposed in Figure 4.12, which increases the distance between the elements of the uniform array designed in Chapter 3, doesn't work.

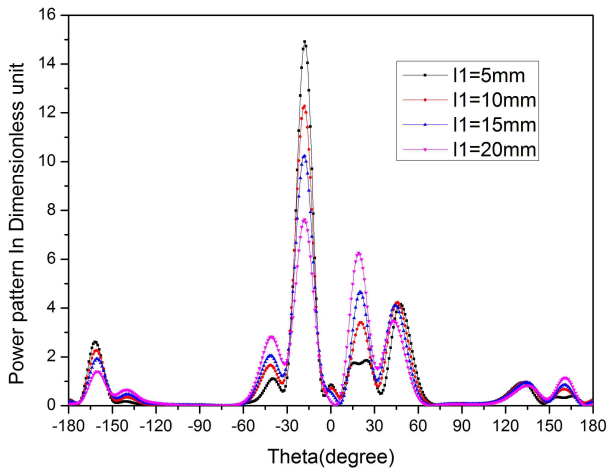

Figure 4.18: H-plane Radiation pattern under the beamsteering mechanism of the narrow-wall longitudinal-slot array.

4.4.2 E-plane Beam-steering

To accomplish beam-steering in the plane orthogonal to the H-plane of the narrow-wall longitudinal-slot array antenna, the easiest and most realizable way is to put two identical antennas aligned with certain distance d between the centers of these two waveguides, as shown in Figure 4.19. The input phase of the first antenna is set to be 0^o. By either moving the antennas or varying the phase of the input of the second antenna β, we can move the beam on the plane orthogonal to the H-plane of the narrow-wall longitudinal-slot array antenna.

From Equation 4.1, we found the expression for the array factor of the two antennas array.

$$AF = \frac{sin\ (\frac{2}{2}(2\pi\frac{d}{\lambda}sin(\phi)+\beta))}{sin\ (\frac{1}{2}\ (2\pi\frac{d}{\lambda}sin(\phi)+\beta))} \tag{4.5}$$

From Equation 4.5, we conclude that by changing d and β, we can change the expression for the array factor. Therefore, the direction of the main beam as well as

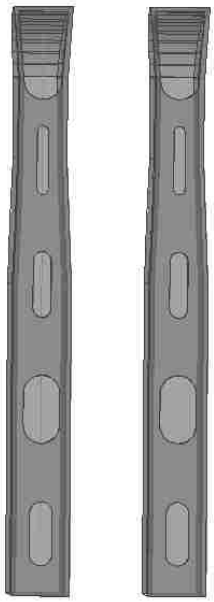

Figure 4.19: Beamsteering mechanism of the narrow-wall longitudinal-slot array.

the peak gain is changed.

Figure 4.20 shows the radiation pattern on the plane cut orthogonal to H-plane and passing through $\theta = -15^o$ line whlie gradually changing the phase difference between the two antennas. We conclude that the beam is moving on the plane cut orthogonal to H-plane and passing through $\theta = -15^o$ line while electrically varying the phase of input of the second antenna.

Figure 4.21 shows shows the radiation pattern on the plane cut orthogonal to H-plane and passing through $\theta = -15^o$ line whlie changing the distance between the centers of the two antennas. We conclude that the beam is moving on the plane cut orthogonal to H-plane and passing through $\theta = -15^o$ line while moving the antennas.

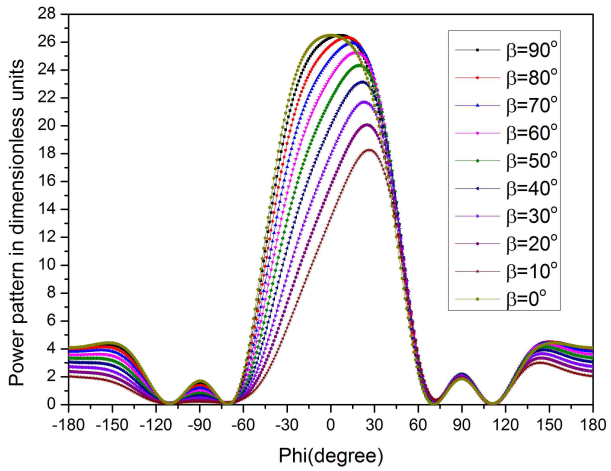

Figure 4.20: Radiation pattern of the Beamsteering mechanism of the narrow-wall longitudinal-slot array on the plane cut orthogonal to H-plane and passing through $\theta = -15^o$ line.

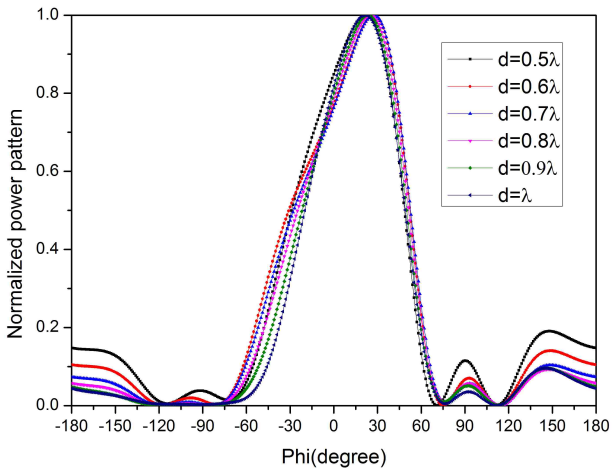

Figure 4.21: Radiation pattern of the Beamsteering mechanism of the narrow-wall longitudinal-slot array on the plane cut orthogonal to H-plane and passing through $\theta = -15^o$ line.

Chapter 5

Experimental Results

The experiments were conducted in the S-band, at 3.17GHz. In the experiments, a narrow-wall longitudinal-slot array without the flare in the narrow wall of the waveguide was verified. The S-band narrow-wall longitudinal-slot array aligned with the X-band narrow-wall longitudinal-slot array is shown in Figure 5.1.

Theoretically, the narrow-wall flare in a rectangular waveguide only affects the power density inside the guide and has no effect on the propagating dominant mode structure, as long as the maximum dimension achieved by the narrow wall of the waveguide still only supports the dominant (TE_{10}) mode and not any higher order modes.

Figure 5.1: the S-band narrow-wall longitudinal-slot array (right) aligned with the X-band narrow-wall longitudinal-slot array (left).

Figure 5.3 shows the experimental set-up used to measure the reflection coefficients of the S-band narrow-wall longitudinal-slot array shown in Figure 5.1.

Figure 5.2: Experimental set-up for measuring reflection coefficient using the network analyzer.

The absorber in Figure 5.2 is placed in front of the narrow-wall longitudinal-slot array so that all the radiated power will be absorbed instead of affecting the antenna itself. We set the frequency sweep range to be from 2.5 GHz to 4 GHz, and the sampling number is 200.

Figure 5.3 shows the result obtained directly from the screen of the network analyzer. The magnitude of S11 for the narrow-wall longitudinal-slot array antenna at 3.17GHz is approximately -33dB.

Figure 5.4 compares the magnitude of the reflection coefficients obtained from the HFSS simulations and experiments, and there is good agreement between the theoretical analysis and experiments.

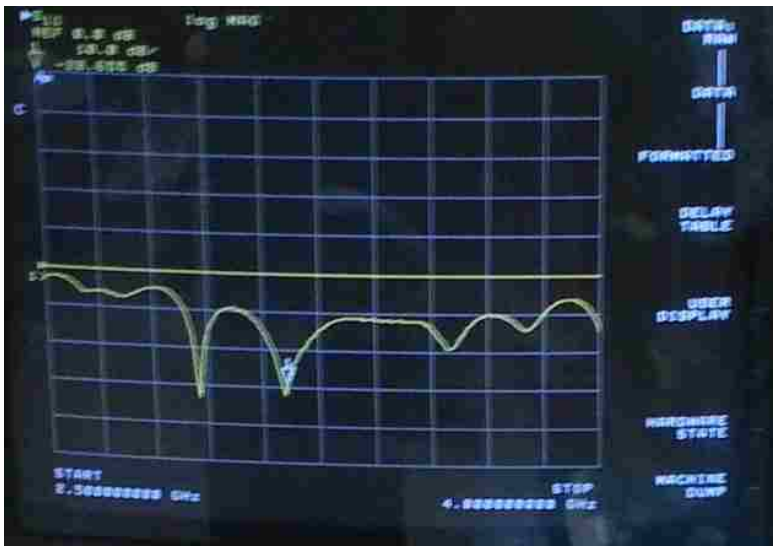

Figure 5.3: Experimental results From the screen of the network analyzer.

Figure 5.5 shows the experimental set up used to measure H-plane radiation pattern of the S-band narrow-wall longitudinal-slot array antenna. Similarly, Figure

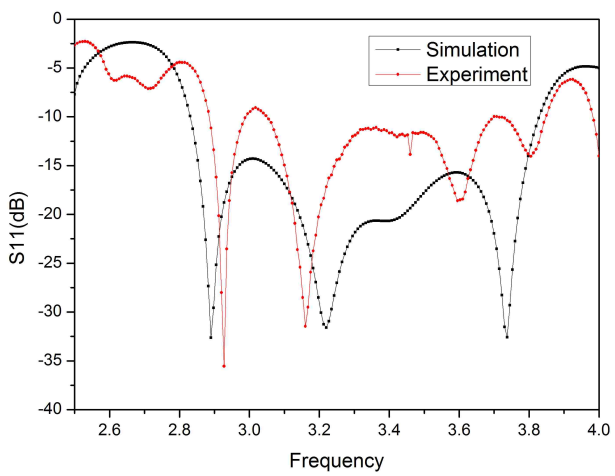

Figure 5.4: the magnitude of the reflection coefficients obtained from the HFSS simulations and experiments.

5.6 and 5.7 show the experimental set up used to measure H-plane and the one that is orthogonal to the H-plane and passing through the $\theta = -15^o$ line shown in Figure 5.8). The description for the radiation pattern measurement system is as follows.

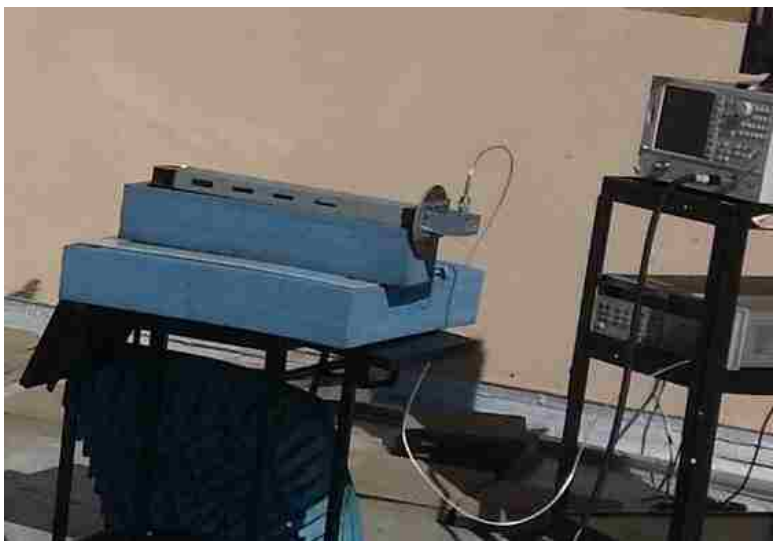

Figure 5.5: Experimental set-up for measuring the H-plane radiation pattern of S-band narrow-wall longitudinal-slot array antenna.

The receiving antenna is a standard gain horn antenna and is mounted on a fixed axis as shown in Figure 5.10. The transmitting antenna is the antenna model under test and is mounted on a compass. In Figure 5.5 and 5.6 the testing model of the antenna design is fixed on a piece of absorber. The antenna, as well as the absorber is placed horizontally as shown in Figure 5.5 and 5.6, so that while rotating the antenna, as well as the absorber, the values of the angles can be read from the compass. However, in Figure 5.7, the testing model is just vertically mounted on the compass, along with a piece of plastic patch to point to the compass so that the values of the angles can be read.

The minimum distance to ensure that the standard horn antenna is in the far-field range of the testing antenna is computed from Equation 5.1, which turns to be

approximately 3.6m.

$$d = \frac{2D^2}{\lambda} \tag{5.1}$$

where:

D is the largest dimension of the antenna, which is approximately 412mm.

Figure 5.6: Overview of the experimental set-up for measuring the H-plane radiation pattern of S-band narrow-wall longitudinal-slot array antenna.

In Figure 5.7, the standard gain horn antenna is placed nearly onto the ground. The minimal distance to be in the far-field of the testing antenna is 3.6m. Hence, the height difference between the center of the standard horn antenna and the testing model is $3.6 * tan(15^o)$, which is approximately 1m. The rack we used to support the antenna is approximately 0.8m, plus half the length of the testing antenna (0.2m); it's approximately 1m. That's the reason that in Figure 5.7, the standard gain horn antenna is placed near the ground. The two absorbers placed right next to the horn antenna are to block the reflection from some metal obstacle.

Figure 5.7: Experimental set-up for measuring the plane cut that is orthogonal to the H-plane and passing throught the $\theta = -15^o$ line shown in Figure 5.8 radiation pattern of S-band narrow-wall longitudinal-slot array antenna.

Figure 5.8 compares the theoretical and experimental H-plane radiation pattern of the S-band narrow-wall longitudinal-slot array antenna. $\theta = 0^o$ on the horizontal axis of the plot in Figure 5.8 corresponds to the broadside direction of the S-band narrow-wall longitudinal-slot array antenna. From Figure 5.8 we conclude that the maximum beam is at $\theta = -15^o$.

Figure 5.9 compares the theoretical and experimental radiation patterns of the S-band narrow-wall longitudinal-slot array antenna in the plane cut that is orthogonal to the H-plane and passing through the $\theta = -15^o$ line shown in Figure 5.8. $\phi = 0^o$ on the horizontal axis of the plot in Figure 5.9 corresponds to the same spatial point in the 3-D radiation power pattern as $\theta = -15^o$ on the horizontal axis of the plot in Figure 5.8.

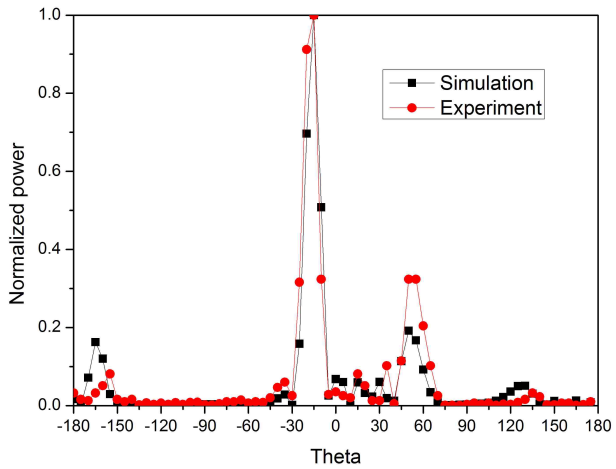

Figure 5.8: H-plane radiation pattern of S-band narrow-wall longitudinal-slot array antenna obtained from the HFSS simulations and experiments.

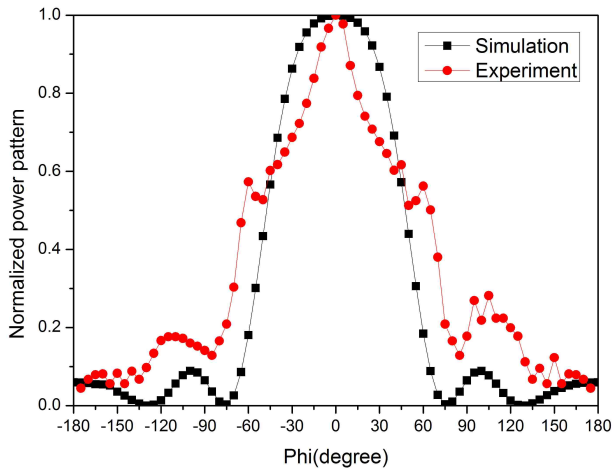

Figure 5.9: Radiation pattern in the plane cut that is orthogonal to the H-plane and passing throught the $\theta = -15^o$ line shown in Figure 5.8 of S-band narrow-wall longitudinal-slot array antenna obtained from the HFSS simulation and experiment.

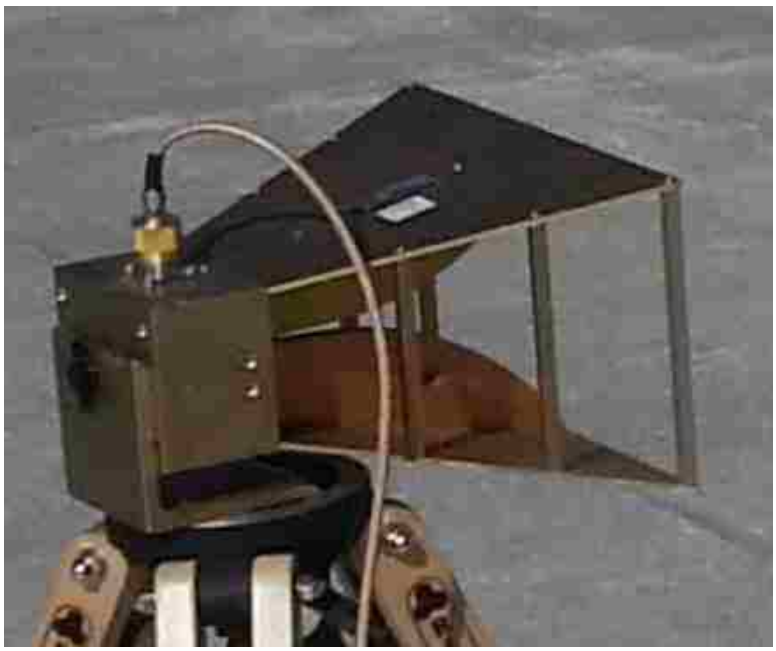

Figure 5.10: Orientation of the standard gain horn antenna in Figure 5.5 and 5.6.

Figure 5.10 and Figure 5.11 shows the orientation of the standard horn antenna in the experimental set-ups shown in Figure 5.5,5.6 and 5.7 for measuring the radiation patterns in the H-plane (Plane cut orthogonal to the H-plane and passing through the $\theta = -15^o$ line)

Figure 5.11: Orientation of the standard gain horn antenna in Figure 5.7.

Chapter 6

Future Work

6.1 Circularly polarized Rectangular Waveguide narrow-wall slot-array

Several designs for circularly polarzied narrow-wall slot-array antennas have been proposed in Chapter 4 section 4. the structure in Figure 4.9 is verified through the help of HFSS. In order to improve our design for high power applications, it is necessary that the number of elements of the circularly polarized antenna array be increased.

Note that, in the structure in Figure 4.9, the distance between the adjacent elements is $\sqrt{2}d$ (d is the distance between the adjacent elements in the original uniform array). The maximum length in the original narrow-wall longitudinal-slot array design is approximately $5d$. So the maximum number of elements in the structure in Figure 4.16 is 4. It means that we can place 4 pairs of narrow-wall longitudinal-slot radiators orthogonal to each other to form a new circularly polarized antenna array.

The method introduced by Chapter 3 should be applied here to find a new 8 ele-

ments narrow-wall longitudinal-slot array, and based on this new design, the structure in Figure 4.9 should be applied and verified to see if the design works for circularly polarized antenna for high power applications.

Similarly, structures in Figure 4.10 and 4.11 should be verified and optimized for high power applications.

6.2 Beam steering capability

In Chapter 4, Section 3, we discussed the beam steering capability of the S-band narrow-wall longitudinal-slot array. However, the results of H-plane beam-steering aren't as inspiring as those of the plane orthogonal to H-plane.

Since the design is based on a air-filled metal rectangular waveguide, it is difficult to change the distance between the adjacent apertures and the progress phase shift between the individual elements. In other words, the array factor is difficult to change. We'd like to do further research on the possibility of changing the radiation pattern of single element by placing varies shapes of patches to change the radiating shapes of the slots and changing the array factor at the same time.

However, due to the aperture of the slots in the narrow-wall longitudinal-slot array design, there isn't very much room left for the manipulation. The capability of H-plane beam-steering may not be as inspiring as the one of the plane orthogonal to the H-plane, as we expected.

6.3 Modified narrow-wall longitudinal-slot array for higher gain

Although the gain of the narrow-wall longitudinal-slot array is smaller compared to the double-narrow-wall slot-array, its structural simplicity is its advantage. Therefore, it is worth seeing whether the gain of the narrow-wall longitudinal-slot array can be improved by slightly increasing its structural complexity. Taking the broad dimension of the waveguide into account might achieve this.

As the broad dimension of the waveguide varies, the guide wavelength changes even for the same frequency. As a result, the progressive phase shift is no longer constant if the distance between adjacent elements stays the same. It is obvious that the distance has to be redesigned based on the change of broad dimension of the waveguide. And within the same required maximum length, the optimal number of elements is no longer 5 and the fraction of power radiated by each element is no longer the same as the design in Chapter 3. Note that, the complexity can be increased if the broad wall taper is not linear.

A modified configuration of narrow-wall longitudinal-slot array for higher gain may look like the structure shown in Figure 6.1.

Figure 6.1: Modified narrow-wall longitudinal-slot array for higher gain.

References

[1] N.R. Devarapalli. *Rectangular waveguide narrow-wall longitudinal-aperture antenna arrays for high power applications*. Ph.d dissertation, University of New Mexico, Albuquerque, New Mexico, August 2009.

[2] C.E. Baum. Sidewall waveguide slot antenna for high power. Sensor and Simulation Notes, Note 503, August 2005.

[3] C.D. Taylor and D.V. Giri. Canonical examples of hpm radiation systems. *High-Power Microwave Systems and Effects*, ch.3:pp.61–110, 1994.

[4] N.R. Devarapalli, C.E. Baum, C.G. Christodoulou, and E. Schamiloglu. A fan-beam radiator using waveguide's narrow wall for horizontal polarization and high power. *Electromagnetic Compatibility, IEEE Transactions on*, Vol.53(2):pp.380–389, May 2011.

[5] A.F. Stevensen. Theory of slots in rectangular wave-guides. *Appl. Phys.*, Vol.19:pp.24–38, Jan 1948.

[6] H. Jasik, editor. *Antenna Engineering Handbook*. McGraw-Hill Companies, Incorporated, 1961.

[7] R.E. Collin. *Field Theory of Guided Waves*. The Institute of Electrical and Electronics Engineers, Inc., New York, 1991.

[8] K.S.H. Lee, editor. *EMP interation:Principles, techniques, and reference data*. "table 14. Aperture Polarizabilities". Hemisphere Publishing Corp., Washington, DC, 1986.

[9] C.A. Balanis. *Antenna Theory: Analysis and Design, 3rd Edition*. Wiley, 2005.

[10] D.M. Pozar. *Microwave Engineering*. Wiley John and Sons, New York, 2005.

[11] L.I. Berger. *CRC Handbook of Chemistry and Phsics*, chapter 15. Practical Laboratory Data. "Table 1. Dielectric strenght of gases". CRC Press/Taylor and Francis, Boca Raton, FL, internet version 2009 edition, 2009.

[12] J.A. Rees, editor. *Electrical Breakdown in Gases*. "Figure 3. Calculated (x) and observed (o) spaking potentials in air". John Wiley + Sons, New York, 1973.

[13] M. Armstrong and N. Alexopoulos. On the design of a circularly polarized waveguide narrow wall linear array. *Antennas and Propagation, IEEE Transactions on*, Vol.23(2):pp.244 – 250, Mar 1975.

[14] G. Montisci. Design of circularly polarized waveguide slot linear arrays. *Antennas and Propagation, IEEE Transactions on*, Vol.54(10):pp.3025 –3029, Oct. 2006.